REPORT NO.
UCB/SEMM-98/05

STRUCTURAL ENGINEERING
MECHANICS AND MATERIALS

FORMULATION AND FINITE ELEMENT IMPLEMENTATION OF A MULTIPLICATIVE MODEL OF COUPLED PORO-PLASTICITY AT FINITE STRAINS UNDER FULLY SATURATED CONDITIONS

BY

F. ARMERO

MARCH 1998

DEPARTMENT OF CIVIL ENGINEERING
UNIVERSITY OF CALIFORNIA
BERKELEY, CALIFORNIA

Formulation and Finite Element Implementation of a Multiplicative Model of Coupled Poro-Plasticity at Finite Strains under Fully Saturated Conditions

by

F. ARMERO

Structural Engineering, Mechanics and Materials
Department of Civil and Environmental Engineering
University of California, Berkeley CA 94720, USA
armero@ce.berkeley.edu

Abstract

We present in this paper the formulation and numerical analysis of a finite deformation model of coupled poro-plasticity. Fully saturated conditions are assumed. The model is based on a multiplicative decomposition of the deformation gradient in elastic and plastic parts, together with an additive elastoplastic decomposition of the fluid content. The final relations describing the evolution of the different fields are then obtained in the thermodynamic framework furnished by the principle of maximum plastic dissipation. The particular case of an associated Drucker-Prager model in effective stresses is considered as a model example. A complete characterization of the dissipative structure of the problem of evolution is described through the derivation of an a-priori stability estimate. We describe in detail the finite element implementation of the model in the context of staggered algorithms for the solution of the physically coupled problem. Finally, we present representative numerical simulations to illustrate the features of the proposed models. In particular, the case of strain localization in globally undrained conditions is studied in the proposed framework.

KEY WORDS: elastoplasticity; porous media; finite element method; staggered schemes; strain localization under undrained conditions.

1. Introduction

The study of the deformation of porous media is of the main interest due to its numerous practical applications. Perhaps the most important of all corresponds to the modeling of the response of soils in geomechanics. In this context, we commonly have the presence of a fluid, typically water, flowing through the pore space of the solid, with different ranges of saturation. In general, the coupling that occurs between the deformation of the solid skeleton and the fluid flow changes significantly the nature of the problem. This situation is of particular interest in the elastoplastic range, a common case given the characteristics of typical soils. The complete characterization and numerical approximation of the resulting physically coupled system becomes then of the main importance. It is the goal of this paper to address several issues regarding the formulation and numerical simulation of these systems in the finite deformation range under fully saturated conditions.

A fundamental contribution to the field was made by Biot, who in a series of papers formulated a general thermodynamic framework for the modeling of coupled poro-elastic and poro-viscoelastic solids in the infinitesimal range (see BIOT [1941,54,55,56b]), with the extension to the finite deformation case presented in BIOT [1972]. Briefly, this framework is characterized by the description of the fully saturated porous solid in terms of the deformation of the solid's skeleton and the fluid content distribution (fluid mass per unit volume). The resulting boundary-value problem leads to a coupled system of equations involving the equations of balance of momentum and the equation of conservation of fluid mass. A typical consideration in the latter is Darcy's law, characterizing the seepage of the fluid through the solid. We refer to COUSSY [1995] for a recent complete account of the ideas behind this framework, together with some extensions as developed in the references presented therein. We also note the close relation of this framework with the study of stress assisted diffusion of solvents in solids, although the two bodies of literature seem to be unconnected to a large extend. We refer to GOVINDJEE & SIMO [1991] for a representative example involving a finite viscoelastic solid. The main goal of this paper is to extend the aforementioned framework to accommodate a multiplicative model of finite strain plasticity.

Finite element solutions of elastic consolidation problems in the infinitesimal range can be found in SANDHU & WILSON [1969], BOOKER & SMALL [1975], and CHRISTIAN [1977], to mention just a few of the earliest works. Similarly, the finite element analysis of infinitesimal elastoplastic consolidation problems has been considered in SMALL et al [1976] and ZIENKIEWICZ & HUMPHESON [1977], among others. The formulation of finite deformation poro-plastic models has been considered by several authors. For example, we refer to the work presented in CARTER et al [1979], and PREVOST [1981], which also included the development of finite element methods for their solution. The framework considered in all these references makes use of a rate form of the constitutive relation. Alternative treatments of finite deformation plasticity in the uncoupled range often consider, however, a multiplicative decomposition of the deformation gradient in an elastic

and a plastic part, together with an underlying hyperelastic response of the material; see MANDEL [1971],SIMO & ORTIZ [1985] and LUBLINER [1986], among many others. These models are becoming more popular due to recent advances in the development of robust numerical integration schemes for their numerical simulation; see WEBER & ANAND [1990], ETEROVICH & BATHE [1990], CUITINHO & ORTIZ [1992] and SIMO [1992]. We refer to SIMO [1994] for a comprehensive account in all these issues.

A recent example of the formulation of a multiplicative finite strain elasto-plastic model of nonlinear consolidation can be found in BORJA & ALARCON [1995], in combination with a mixture-type framework (that is, accounting for e.g. stresses in the fluid and solid). Except for the usual dissipative effects associated with the conduction of fluid mass (following, e.g., Darcy's law), the framework presented by these authors exhibits no irreversible elastoplastic response associated to the evolution of the fully saturated porous space. This situation is to be contrasted with several extensions of the aforementioned Biot's framework that consider an additive elastoplastic decomposition of the fluid content, or related porosity of the solid, in the infinitesimal range. See COUSSY [1995] and BENALLAL & COMI [1997].

We present in this paper a general framework that accommodates these two elastoplastic decompositions in the finite deformation range, that is, an elastoplastic multiplicative decomposition of the deformation gradient and an additive elastoplastic decomposition of the fluid content. The final evolution equations for the different fields are derived in the thermodynamical framework furnished by the principle of maximum plastic dissipation, leading to an associated model in the usual sense. In particular, the role of the pore pressure field, in the case of a barotropic fluid, as conjugate in the dissipation inequality to the plastic change of fluid content is studied in this general finite deformation range. Specifically, the common example of a poro-plastic model in effective stresses is considered. We note the relation of the resulting formulation with the treatments of multiplicative coupled thermo-plasticity presented in SIMO & MIEHE [1992], given the formal analogy of the two problems. See also the discussion in ARMERO & SIMO [1993]. To our knowledge, the current paper is the first to consider the combination of these two known elastoplastic decompositions in the formulation of a coupled finite deformation poro-plastic model.

We describe in detail the implementation of this model in the context of the finite element method. In particular, we consider *staggered methods* for the solution of the resulting physically coupled system. In the context of the coupled solid/fluid interaction system of interest herein, complete reviews of these methods can be found in LEWIS & SCHREFLER [1987], WOOD [1990] (Chapter 8), and ZIENKIEWICZ & TAYLOR [1991] (Chapter 11). We presented in ARMERO & SIMO [1992,93] an analysis of standard staggered methods for coupled thermomechanical problems in the framework of the method of fractional steps (see e.g. YANENKO [1971]). In particular, we identified the breaking of the contractive structure of the problem by the partition underlying standard staggered methods as the cause for their inherent instability. In addition, the analysis identified alternative meth-

ods that preserve this structure, leading to unconditionally stable single-pass staggered algorithms. Noteworthy, the proposed analysis applies to the fully nonlinear finite strain thermo-plastic problem, and apply by analogy to the poro-plastic case of interest herein. We refer also to ARMERO & SIMO [1996] for the development of stable fractional step methods for the MHD equations of fluid mechanics following similar ideas.

Given this formal analogy, we outline only briefly in this paper the extension of these considerations to the finite strain poro-plastic model developed in the first part of the paper. Specifically, two different partitions of the problem are available, both involving two phases, a solid and a fluid phase, corresponding to the solution of the equilibrium equations and fluid mass conservation, respectively. The difference between the two strategies stems from the drained or undrained character of the solid phase, as it can be found in the literature. In particular, staggered algorithms based on a drained solid phase can be found in PARK & FELIPPA [1983] or WOOD [1990], among many others, and on an undrained solid phase in ZIENKIEWICZ et al [1988] for the linear elastic consolidation problem. In fact, the stability of the numerical schemes resulting from an undrained partition of the problem is shown in this last reference through a classical von Neumann analysis of the linearized problem. The results outlined herein show that the undrained split conforms with the dissipative character of the problem of evolution by inheriting an a-priori stability estimate of the exact coupled problem. The stability of the schemes based on this split, with each sub-problem solved with a stable scheme, is then concluded *in the general fully nonlinear finite strain coupled poro-plastic range.*

An outline of the rest of the paper is as follows. Section 2 summarizes the equations governing the deformation and fluid flow in a fully saturated porous media. The finite strain poro-plastic model proposed in this work is developed in Section 3, with the characteristic example given by Drucker-Prager's model in effective stresses described in Section 3.4. We derive in Section 3.5 an a-priori stability estimate for the resulting boundary value problem. The proposed model is then evaluated numerically in representative numerical simulations presented in Section 4. Finally, and after presenting some concluding remarks in Section 5, we describe in Appendix I full details of the finite element implementation of the proposed methods, including return mapping algorithms used in the numerical integration of the proposed finite strain poro-plastic models.

2. The Governing Equations

We summarize in this section the equations governing the evolution of a porous media. The thermodynamical framework first proposed by BIOT [1941,55,72] is considered. In this context, Section 2.1 presents the equations governing the balance of linear and angular momenta, as well as the equation describing the conservation of fluid mass. Crucial to the formulation of the poro-elastoplastic model considered in Section 3 is the characterization

of the dissipation inequality in this general framework. We summarize these issues in Section 2.2. We refer to the recent account in COUSSY [1995] for complete details in the derivation and extensions of the equations presented herein.

2.1. The balance equations

We consider a porous solid occupying a reference placement $\mathcal{B}$ and composed of a skeleton and a fluid flowing through the pore space. The motion of the *solid's skeleton*, consisting of the solid matrix and the (non-occluded) pore space, is characterized by the deformation mapping $\boldsymbol{\varphi} : \mathcal{B} \times [0,T] \to \mathbb{R}^{n_{\text{dim}}}$ ($n_{\text{dim}} = 1, 2$, or 3), for a typical time interval T. As customary, we denote by $\boldsymbol{x} = \boldsymbol{\varphi}(\boldsymbol{X}, t)$ the current position of the skeleton particle $\boldsymbol{X} \in \mathcal{B}$; see Figure 2.1.

The pore space is assumed to be fully saturated with a single fluid phase. The open system defined by the fluid flowing through particles of the porous solid's skeleton can be characterized by the *fluid content* $M : \mathcal{B} \times [0,T] \to \mathbb{R}$ (fluid mass per unit reference volume). The fluid content M is defined in terms of the components of the solid/fluid mixture as

$$M = \rho_w \, \phi_p \, J \, , \tag{2.1}$$

where ρ_w is the current density of the fluid and ϕ_p is the current porosity of the solid. We have introduced in (2.1) the standard notation for the Jacobian

$$J := \det \boldsymbol{F} > 0 \qquad \text{for} \qquad \boldsymbol{F} := \text{GRAD}\, \boldsymbol{\varphi} \, , \tag{2.2}$$

with $\text{GRAD}(\cdot)$ denoting the material gradient with respect to the reference coordinates $\boldsymbol{X}$. The evolution of the deformation $\boldsymbol{\varphi}$ and the fluid content M are governed by the following balance laws.

i. Conservation of fluid mass. Assuming that no volumetric sources of fluid exist, the conservation of fluid mass reads

$$\frac{1}{J}\dot{M} = -\operatorname{div} \boldsymbol{q}_w \, , \tag{2.3}$$

for the material time derivative $\dot{(\cdot)} = \partial(\cdot)/\partial t|_{\boldsymbol{X}}$ (that is, fixing the skeleton particle $\boldsymbol{X}$), the divergence operator $\operatorname{div}(\cdot)$ with respect to the spatial coordinates $\boldsymbol{x} = \boldsymbol{\varphi}(\boldsymbol{X}, t)$, and the flow vector field $\boldsymbol{q}_w : \mathcal{B} \times [0,T] \to \mathbb{R}^{n_{\text{dim}}}$ of fluid mass. Indeed, the rate of change of the fluid mass in the deformed configuration $\boldsymbol{\varphi}(\mathcal{P}_X)$ of any material part $\mathcal{P}_X \subset \mathcal{B}$ of the solid's skeleton (see Figure 2.1) is given by

$$\frac{d}{dt} \int_{\boldsymbol{\varphi}(\mathcal{P}_X)} \rho_w \phi_p \, dv = - \int_{\partial \boldsymbol{\varphi}(\mathcal{P}_X)} \boldsymbol{q}_w \cdot \boldsymbol{n} da \, , \tag{2.4}$$

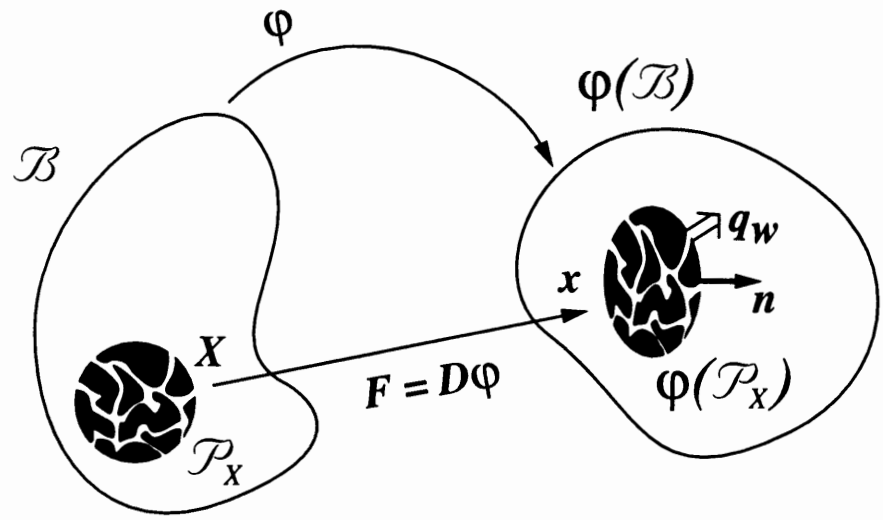

FIGURE 2.1. Problem definition. A porous solid is subjected to a deformation φ of the skeleton and a fluid flow characterized by the flow vector $\boldsymbol{q}_w$.

where $\boldsymbol{q}_w \cdot \boldsymbol{n}$ corresponds to the fluid mass flux across the bounding surface $\partial\boldsymbol{\varphi}(\mathcal{P}_X)$ with unit normal $\boldsymbol{n}$. A standard argument based on Gauss theorem leads to (2.3). In terms of the mixture constituents, we can write

$$\boldsymbol{q}_w = -\rho_w \phi_p (\boldsymbol{v}_w - \boldsymbol{v}) \,, \tag{2.5}$$

for the relative velocity of the fluid $(\boldsymbol{v}_w - \boldsymbol{v})$ with respect to the velocity of the skeleton $\boldsymbol{v} = \dot{\boldsymbol{\varphi}} \circ \boldsymbol{\varphi}^{-1}$. We note, however, that the formulation considered herein does not make use of the fields characterizing the different phases of the mixture and, in particular, of the porosity ϕ_p. Instead, and following BIOT [1941,55,72], the state of the porous solid/fluid system is completely characterized by the two fields $\boldsymbol{\varphi}$ and M, with the addition of other internal variables characterizing its inelastic response, as described in Section 3 below.

The consideration of the Piola transform (see e.g. MARSDEN & HUGHES [1983])

$$\boldsymbol{Q}_w := J\, \boldsymbol{F}^{-1} \boldsymbol{q}_w \qquad \Big(\Longrightarrow J \operatorname{div} \boldsymbol{q}_w = \operatorname{DIV} \boldsymbol{Q}_w \Big) \,, \tag{2.6}$$

for the material divergence operator $\operatorname{DIV}(\cdot)$ (with respect to $\boldsymbol{X}$), leads to

$$\dot{M} = -\operatorname{DIV} \boldsymbol{Q}_w \,, \tag{2.7}$$

the material form of fluid mass balance.

ii. The equilibrium equations. The local equation of equilibrium for the solid-fluid system in the quasi-static limit of interest reads (see BIOT [1955])

$$\operatorname{div} \boldsymbol{\sigma} + \rho \boldsymbol{f} = 0 \,, \tag{2.8}$$

for the *total Cauchy stress tensor* $\boldsymbol{\sigma}$, the external body force $\boldsymbol{f}$ per unit mass (assumed the same for both the fluid and the skeleton), and the apparent density ρ of the porous solid, defined in terms of the mixture constituents by

$$\rho = \phi_p \rho_w + (1 - \phi_p)\rho_s \,, \tag{2.9}$$

for the density ρ_s of the solid phase. As usual, the balance of angular momentum in a non-polar media leads to the symmetry of the total stress $\boldsymbol{\sigma}^T = \boldsymbol{\sigma}$. The material form of equation (2.8) reads

$$\text{DIV}\, \boldsymbol{P} + \rho_o \boldsymbol{f} = 0 \,, \tag{2.10}$$

in terms of the first Piola-Kirchhoff stress tensor $\boldsymbol{P} := J\boldsymbol{\sigma}\boldsymbol{F}^{-T}$ and the reference density

$$\rho_o = \rho\, J \,. \tag{2.11}$$

Equation (2.11) follows through a standard argument imposing the conservation of mass of the solid's skeleton under the action of its deformation $\boldsymbol{\varphi}$ and the corresponding Jacobian J.

2.2. Energy balance and entropy production

Denoting the internal energy density (per unit reference volume of skeleton) of the solid/fluid mixture by $e : \mathcal{B} \times [0, T] \to \mathbb{R}$, the conservation of energy leads to the following local evolution equation under isothermal conditions

$$\frac{1}{J}\dot{e} = \boldsymbol{\sigma} : \boldsymbol{d} + \Big(\boldsymbol{f} \cdot \boldsymbol{q}_w - \text{div}\,[h_w \boldsymbol{q}_w] \Big) \,, \tag{2.12}$$

that is, the rate of change of the internal energy e is given by the power of the total stresses $\boldsymbol{\sigma}$ on the rate of deformation of the skeleton $\boldsymbol{d} := \dot{\boldsymbol{F}}\boldsymbol{F}^{-1}$, plus the contributions of the fluid flow, the last two terms in (2.12). In particular, the *macroscopic* contributions of the fluid flow are given by the extra power done by the external forces $\boldsymbol{f}$ on the relative velocity of the fluid ($\boldsymbol{f} \cdot \boldsymbol{q}_w$), and the rate of energy leaving a particle of the solid's skeleton due to the actual conduction of fluid mass.

A typical example of external loading is furnished by the action of the gravity field, a conservative load defined by the potential $\mathcal{V}_{ext}$

$$\boldsymbol{f} = -\partial_{\varphi} \mathcal{V}_{ext} = \boldsymbol{g} \,, \qquad \text{with} \qquad \mathcal{V}_{ext} = -\boldsymbol{\varphi} \cdot \boldsymbol{g} + \text{constant} \,, \tag{2.13}$$

for the gravity acceleration $\boldsymbol{g} \in \mathbb{R}^{n_{\text{dim}}}$. The contribution to the energy change due to the conduction of the fluid mass is represented by the last term in (2.12), with h_w denoting the enthalpy of the fluid (per unit fluid mass) transported by the fluid mass flow vector $\boldsymbol{q}_w$.

Similarly, the postulate of positive entropy production (second law of thermodynamics) can be written in terms of the entropy density of the solid/fluid mixture (per unit reference volume of the solid's skeleton), denoted by $\eta : \mathcal{B} \times [0, T] \to \mathbb{R}$, as

$$\frac{1}{J}\Gamma_{entr} := \frac{1}{J}\frac{d\eta}{dt} + \text{div}\,[s_w \boldsymbol{q}_w] \geq 0 \,, \tag{2.14}$$

for the rate of entropy production Γ_{entr} (per unit reference volume), with the last term representing the entropy of the fluid s_w (per unit fluid mass) leaving a given skeleton particle. Isothermal conditions are again assumed in (2.14). In fact, denoting by T_o the constant absolute temperature of the mixture and defining

$$\psi := e - T_o\eta \ , \qquad \text{and} \qquad \mu_w := h_w - T_o s_w \ , \tag{2.15}$$

for the *free energy of the porous solid* ψ and the *free enthalpy of the fluid* μ_w (or fluid's chemical potential), we can write the total dissipation $\mathcal{D} := T_o\Gamma_{entr}$ as

$$\mathcal{D} = \underbrace{\boldsymbol{\tau} : \boldsymbol{d} + \mu_w \dot{M} - \dot{\psi}}_{\mathcal{D}_{int}} \underbrace{- J\boldsymbol{q}_w \cdot \nabla\left[\mu_w + \mathcal{V}_{ext}\right]}_{\mathcal{D}_{cond}} \geq 0 \ , \tag{2.16}$$

for the Kirchhoff stresses $\boldsymbol{\tau} = J\boldsymbol{\sigma}$ and the spatial gradient $\nabla(\cdot)$ (with respect to the spatial coordinates $\boldsymbol{x}$), after combining (2.12) and (2.14) with the Piola transform (2.6).

Darcy's law furnishes an example for the definition of the fluid flow vector $\boldsymbol{q}_w$. In the notation introduced above and given the expression (2.16) of $\mathcal{D}_{cond}$, it is given by

$$\boldsymbol{q}_w = -\rho_w^2 \boldsymbol{k} \nabla(\mu_w + \mathcal{V}_{ext}) \ , \tag{2.17}$$

with a positive semi-definite permeability tensor $\boldsymbol{k}$; see Remark 2.1.1 below. This property conforms with the observation of non-negative entropy production due to the seepage process (that is, $\mathcal{D}_{cond} \geq 0$).

The common argument imposing separately a non-negative entropy production due to the internal processes occurring in the porous solid (see e.g. TRUESDELL & NOLL [1965]) leads to the reduced Clausius-Planck inequality

$$\boxed{\mathcal{D}_{int} = \boldsymbol{\tau} : \boldsymbol{d} + \mu_w \dot{M} - \dot{\psi} \geq 0 \ .} \tag{2.18}$$

We note the conjugate character of the fluid content M and the fluid's free enthalpy μ_w.

The case of interest herein consists of a barotropic fluid whose state is characterized by a *pore pressure field* $p : \mathcal{B} \times [0,T] \to \mathbb{R}$ and the constitutive relation

$$\rho_w = \hat{\rho}_w(p) \ . \tag{2.19}$$

In this case, the *free enthalpy* μ_w is given by

$$\mu_w = \hat{\mu}_w(p) = \int^p \frac{d\eta}{\hat{\rho}_w(\eta)} \ , \tag{2.20}$$

Furthermore, Darcy's law reduces in this case to the common expression

$$\boldsymbol{q}_w = -\rho_w \boldsymbol{k} \left[\nabla p - \rho_w \boldsymbol{g}\right] \ , \tag{2.21}$$

in terms of the pore pressure p. We note that the convention taken in this paper considers positive tensile stresses $\boldsymbol{\sigma}$, and positive pore pressure p.

Remarks 2.1.

1. The spatial permeability tensor $\boldsymbol{k}$ in (2.17) and (2.21) is given by

$$\boldsymbol{k} = J\boldsymbol{k}_o \,, \tag{2.22}$$

in terms of the positive semi-definite tensor $\boldsymbol{k}_o$ specified per unit reference volume of the porous solid. We have $\boldsymbol{k}_o = \boldsymbol{k}_{i_o}/\eta_{w_o}$ for the *intrinsic permeability of the porous space* $\boldsymbol{k}_{i_o}$ (units of reference length^2) and the viscosity η_{w_o} of the fluid or, alternatively, $\boldsymbol{k}_o = \boldsymbol{k}_{h_o}/\gamma_{w_o}$ for the *hydraulic permeability* parameter (units of reference length per unit of time) and the specific weight $\gamma_{w_o} = \rho_{w_o} g$ of the fluid. See e.g. BEAR [1972] for more details and typical values. Note that the positive semi-definiteness of $\boldsymbol{k}$ follows, since $J > 0$. The combination of the Piola transform (2.6) and the relation $\nabla(\cdot) = \boldsymbol{F}^{-T}\,\mathrm{GRAD}(\cdot)$ leads to the convected expression

$$\boldsymbol{Q}_w = -\rho_w^2 \boldsymbol{K}_o\,\mathrm{GRAD}(\mu_w + \mathcal{V}_{ext}) \qquad \text{with the relation} \quad \boldsymbol{k}_o = \boldsymbol{F}\boldsymbol{K}_o\boldsymbol{F}^T \,, \tag{2.23}$$

for the material flow vector $\boldsymbol{Q}_w$. The positive semi-definiteness of $\boldsymbol{K}_o$ follows from the same property of $\boldsymbol{k}_o$.

2. The general boundary-value problem of coupled poro-plasticity is defined by the balance equations (2.7) and (2.10) (or, equivalently, by their spatial counterparts (2.3) and (2.8)), supplemented by the constitutive relations developed in the following sections, and the proper initial and boundary conditions. For example, the boundary conditions

$$\boldsymbol{\varphi} = \bar{\boldsymbol{\varphi}} \quad \text{on} \quad \partial_\varphi\mathcal{B} \subset \partial\mathcal{B} \,, \qquad \text{and} \qquad \boldsymbol{P}\boldsymbol{N} = \bar{\boldsymbol{T}} \quad \text{on} \quad \partial_T\mathcal{B} \subset \partial\mathcal{B} \,, \tag{2.24}$$

are usually considered, involving an imposed deformation $\bar{\boldsymbol{\varphi}}$ and traction vector $\bar{\boldsymbol{T}}$ on different parts of the boundary $\partial\mathcal{B}$ with material unit normal $\boldsymbol{N}$. The relations

$$\partial_\varphi\mathcal{B} \cap \partial_T\mathcal{B} = \emptyset \qquad \text{and} \qquad \overline{\partial_\varphi\mathcal{B} \cup \partial_T\mathcal{B}} = \partial\mathcal{B} \,, \tag{2.25}$$

in each spatial component are required for a well-posed problem. Similarly, the boundary conditions

$$p = \bar{p} \quad \text{on} \quad \partial_p\mathcal{B} \subset \partial\mathcal{B} \qquad \text{and} \qquad \boldsymbol{Q}_w \cdot \boldsymbol{N} = \bar{Q}_w \quad \text{on} \quad \partial_Q\mathcal{B} \subset \partial\mathcal{B} \,, \tag{2.26}$$

on the pore pressure field are usually imposed with requirements similar to (2.25). In particular, the case of an impervious boundary is recovered by setting the nominal fluid flux $\bar{Q}_w = 0$ in $(2.26)_2$. □

3. A Multiplicative Poro-Elasto-Plastic Model

The governing equations summarized in the previous section need to be supplemented with the constitutive relations characterizing the elastic and inelastic responses of the porous solid, in general. The actual relations between the stresses and the deformation and fluid content fields through the free energy ψ need to be developed. We formulate in this section a general finite strain poro-elasto-plastic model. To this purpose, Section 3.1 introduces the assumed elastoplastic decompositions in this finite deformation range, with the evolution for the different fields developed in Section 3.2 and 3.3 for the elastic and plastic contributions, respectively. The model example furnished by a generalized Drucker-Prager model in Biot effective stresses is presented in Section 3.4. Finally, Section 3.5 describes the dissipative structure of the resulting problem of evolution.

3.1. The elasto-plastic decompositions

We consider a *multiplicative* decomposition of the deformation gradient

$$\boxed{\boldsymbol{F} = \boldsymbol{F}^e \boldsymbol{F}^p \,,} \tag{3.1}$$

identifying the plastic part of the deformation gradient $\boldsymbol{F}^p$ whose general evolution is to be specified, and the elastic part of the deformation gradient $\boldsymbol{F}^e$ defining the intermediate configuration together with the mechanical elastic response of the material. See Figure 3.1 for an illustration.

Similarly, the scalar field of the fluid content M is assumed decomposed *additively* as

$$\boxed{M = M^e + M^p \,,} \tag{3.2}$$

in elastic and plastic parts, respectively. We note that the additive decomposition (3.2) is consistent with the extensive nature of the fluid content M, a *scalar* field. As given by the constitutive relations developed in the forthcoming sections, it identifies the reversible M^e and irreversible M^p changes of the fluid content in the porous solid.

The multiplicative decomposition (3.1) was first considered in LEE & LIU [1967] and LEE [1969], and is nowadays common in modern treatments of uncoupled finite strain plasticity; see the complete review in SIMO [1994] and references therein. The additive decomposition (3.2) of the fluid content has been considered in COUSSY [1995], and more recently in BENALLAL & COMI [1997], in the infinitesimal range. The analogy of the proposed treatment of the coupled problem of interest with the formulations of finite strain thermoplasticity considered in SIMO & MIEHE [1992] and ARMERO & SIMO [1993] is also to be noted. See Section 3.5 below for additional details on this analogy.

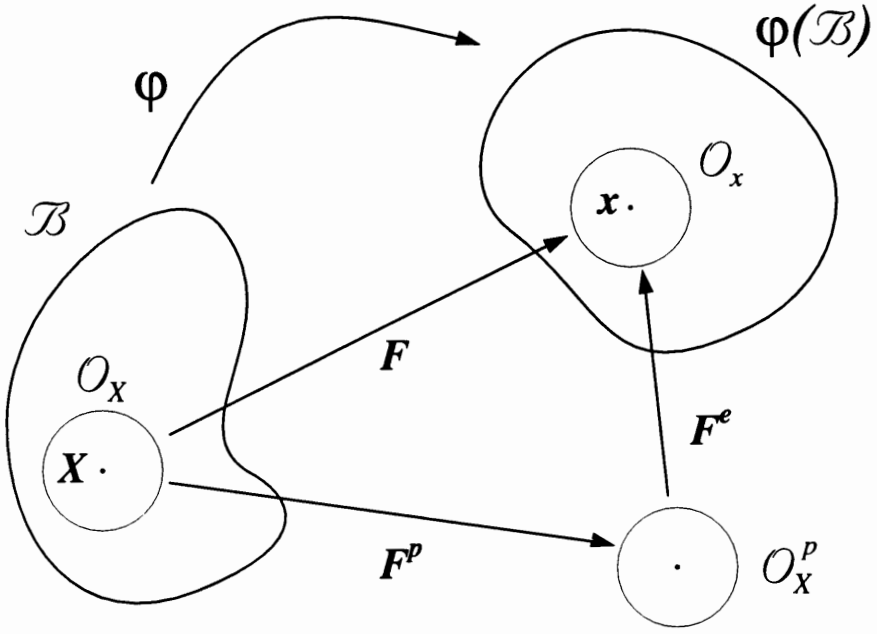

FIGURE 3.1. Multiplicative decomposition of the deformation gradient $\boldsymbol{F} = \boldsymbol{F}^e\boldsymbol{F}^p$ in elastic and plastic parts, characterizing *locally* the intermediate configuration $\mathcal{O}_X^p$.

3.2. The elastic constitutive relations

The reversible response of the solid is given by the free energy function ψ, assumed to be a function of the elastic fields identified in the previous section. In this way, we write

$$\psi = \hat{\psi}(\bar{\boldsymbol{C}}^e, M^e, \alpha) \,, \tag{3.3}$$

where, for simplicity, we have considered a single scalar internal variable α characterizing the (isotropic) hardening response of the material. The dependence of the free energy function on the elastic right Cauchy-Green tensor $\bar{\boldsymbol{C}}^e$ rather than the elastic part of the deformation gradient $\boldsymbol{F}^e$ follows from a standard argument based on material frame indifference with respect to superimposed rigid body motions to the current configuration (see e.g. TRUESDELL & NOLL [1965]).

A classical argument, known as Coleman's method, and based on the imposition of the reduced dissipation inequality (2.18) (see e.g. TRUESDELL & NOLL [1965]), leads to the following elastic relations

$$\bar{\boldsymbol{S}} = 2\partial_{\bar{\boldsymbol{C}}^e}\psi \qquad \text{and} \qquad \mu_w = \partial_{M^e}\psi \,, \tag{3.4}$$

for the second Piola-Kirchhoff stress tensor $\bar{\boldsymbol{S}} := \boldsymbol{F}^{e-T}\boldsymbol{\tau}\boldsymbol{F}^{e-1}$ in the intermediate configuration. After some algebraic manipulations, the internal dissipation (2.18) reduces then to

$$\mathcal{D} = \bar{\boldsymbol{C}}^e\bar{\boldsymbol{S}} : \bar{\boldsymbol{L}}^p + q\dot{\alpha} + \mu_w\,\dot{M}^p \qquad \text{where} \qquad \bar{\boldsymbol{L}}^p = \dot{\boldsymbol{F}}^p\boldsymbol{F}^{p-1} \,, \tag{3.5}$$

and $q := -\partial_\alpha \psi$. The first two terms are common in uncoupled mechanical plasticity theories and capture the inelastic response associated to the plastic strains and hardening of the solid skeleton. We observe the addition to the local dissipation of a term proportional to the irreversible change of the fluid content.

Of interest for the developments presented below is the consideration of the isotropic case characterized by the dependence of the free energy ψ on the left Cauchy-Green tensor $\boldsymbol{b}^e$, due to the invariance relative to superimposed rigid body motions on the intermediate configuration. The constitutive relation $(3.4)_1$ is then given equivalently by

$$\boldsymbol{\tau} = 2\boldsymbol{b}^e \partial_{\boldsymbol{b}^e} \psi \,, \tag{3.6}$$

in this case; see e.g. TRUESDELL & NOLL [1965]. After using the relation

$$-\tfrac{1}{2}\boldsymbol{\pounds}_{\boldsymbol{v}} \boldsymbol{b}^e = \boldsymbol{F}^e \,\mathrm{sym}\left[\bar{\boldsymbol{L}}^p\right] \boldsymbol{F}^{eT} \,, \qquad \text{where} \qquad \boldsymbol{\pounds}_{\boldsymbol{v}} \boldsymbol{b}^e := \boldsymbol{F} \frac{d}{dt}\left[\boldsymbol{F}^{-1} \boldsymbol{b}^e \boldsymbol{F}^{-T}\right] \boldsymbol{F}^T \,, \tag{3.7}$$

(that is, the Lie derivative $\boldsymbol{\pounds}_{\boldsymbol{v}} \boldsymbol{b}^e$ of the elastic left Cauchy-Green strain tensor $\boldsymbol{b}^e$), the dissipation (3.5) is given by

$$\mathcal{D} = \boldsymbol{\tau} : (-\tfrac{1}{2}\boldsymbol{\pounds}_{\boldsymbol{v}} \boldsymbol{b}^e \; \boldsymbol{b}^{e-1}) + q\dot{\alpha} + \mu_w \; \dot{M}^p \,, \tag{3.8}$$

in this isotropic case. We refer to SIMO [1994] for a comprehensive account of the details of the above calculations involving the different mechanical tensor fields.

Remark 3.1. As discussed in the Appendix I, the finite element solution of the resulting boundary value problem uses the pressure field p rather than the fluid content M as the primary variable for the numerical implementation. With this motivation, we define the potential

$$\hat{\chi}(\bar{\boldsymbol{C}}^e, p, \alpha) := -\max_{M^e} \{\mu_w(p) M^e - \hat{\psi}(\bar{\boldsymbol{C}}^e, M^e, \alpha)\} \,, \tag{3.9}$$

following a similar strategy as in BIOT [1972] for poro-elasticity, that is, the Legendre transform of the free energy function in the conjugate fields $\{M^e, p\}$. Given the definition (3.9), the constitutive relations (3.4) read

$$\bar{\boldsymbol{S}} = 2\partial_{\bar{\boldsymbol{C}}^e} \chi \qquad \text{and} \qquad M^e = -\rho_w \; \partial_p \chi \,, \tag{3.10}$$

after using the definition (2.20) for the free enthalpy of the fluid. □

3.3. The plastic evolution equations

The inelastic response of the material is characterized by a yield criterion

$$\Phi(\boldsymbol{\tau}, q, \mu_w) \leq 0 \,, \tag{3.11}$$

defining the admissible elastic domain in terms of the thermodynamical forces identified by the reduced dissipation inequality (2.18). The isotropic case, given the dependence on the spatial Kirchhoff stresses of Φ, has been considered in (3.11).

The maximization of the dissipation (2.18) for fixed rates of the plastic internal variables leads to the plastic evolution equations

$$\boxed{\left.\begin{aligned} \pounds_{\boldsymbol{v}} \boldsymbol{b}^e &= -2\gamma\, \partial_{\boldsymbol{\tau}} \Phi\, \boldsymbol{b}^e \,, \\ \dot{\alpha} &= \gamma\, \partial_q \Phi \,, \\ \dot{M}^p &= \gamma\, \partial_{\mu_w} \Phi \,, \end{aligned}\right\}} \tag{3.12}$$

for the plastic multiplier γ satisfying the complementary Kuhn-Tucker loading/unloading conditions

$$\gamma \geq 0 \,, \quad \Phi \leq 0 \,, \quad \gamma\Phi = 0 \,, \tag{3.13}$$

and the consistency condition

$$\gamma\dot{\Phi} = 0 \,, \tag{3.14}$$

during plastic loading. Equations $(3.12)_1$ and $(3.12)_2$ correspond to the flow rule and hardening law, respectively, whereas $(3.12)_3$ identifies the irreversible change in fluid content associated to the change in state of the fluid (through μ_w). We refer to Section 3.4 below for a complete discussion of this equation in the context of an effective stress model. As usual, the proper use of the principle of maximum plastic dissipation requires the convexity of the admissible elastic domain defined by the yield surface; we refer again to SIMO [1994] for complete details.

Typical yield surfaces $\Phi(\boldsymbol{\tau}, \mu_w, q)$ are defined in the form

$$\Phi(\boldsymbol{\tau}, q, \mu_w) = \widetilde{\Phi}(\boldsymbol{\tau}, \mu_w) - [\tau_{yo} - q] \,, \tag{3.15}$$

for an initial yield parameter $\tau_{yo} > 0$ and a (positively) homogeneous function $\widetilde{\Phi}(\boldsymbol{\tau}, \mu_w)$, that is,

$$\widetilde{\Phi}(\lambda\boldsymbol{\tau}, \lambda\mu_w) = \lambda\, \widetilde{\Phi}(\boldsymbol{\tau}, \mu_w) \qquad \forall\lambda \in \mathbb{R}_+ \,, \quad \text{and} \quad \forall\boldsymbol{\tau} \,, \mu_w \,, \tag{3.16}$$

implying

$$\widetilde{\Phi}(\boldsymbol{\tau}, \mu_w) = \boldsymbol{\tau} : \partial_{\boldsymbol{\tau}} \widetilde{\Phi} + \mu_w\, \partial_{\mu_w} \widetilde{\Phi} \,, \tag{3.17}$$

by the Euler theorem of homogeneous functions. An example of yield criteria of the form (3.15) is presented in Section 3.4 below. The intrinsic dissipation (2.18) reads in this case

$$\begin{aligned} \mathcal{D}_{int} = \boldsymbol{\tau} : & \underbrace{\left(\gamma\, \partial_{\boldsymbol{\tau}} \widetilde{\Phi}\right)}_{=-\frac{1}{2}\pounds_{\boldsymbol{v}} \boldsymbol{b}^e\, \boldsymbol{b}^{e-1}} + \mu_w \underbrace{\left(\gamma\, \partial_{\mu_w} \widetilde{\Phi}\right)}_{=\dot{M}^p} + q\, \underbrace{\gamma}_{=\dot{\alpha}} \\ &= (\widetilde{\Phi} + q)\, \gamma = \tau_{yo}\, \gamma \geq 0 \,, \end{aligned} \tag{3.18}$$

due to the Kuhn-Tucker conditions (3.13). The proposed multiplicative model conforms then with the dissipation inequality (2.18), a direct consequence of its maximally dissipative character.

Remarks 3.2.

1. For the common case involving a barotropic fluid, as defined by (2.19), we observe that the evolution of the plastic fluid content $(3.12)_3$ can be written equivalently as

$$\dot{M}^p = \gamma \rho_w \partial_p \Phi_{baro} \ , \tag{3.19}$$

for $\Phi_{baro}(\boldsymbol{\tau}, q, p) = \Phi(\boldsymbol{\tau}, q, \mu_w(p))$.

2. General anisotropic models in terms of the Mandel stresses $\boldsymbol{\Sigma} := \bar{\boldsymbol{C}}^e \bar{\boldsymbol{S}}$, as identified by (3.5), follow similarly. In particular, the flow rule $(3.12)_1$ usually takes the general form

$$\bar{\boldsymbol{L}}^p = \gamma \partial_{\boldsymbol{\Sigma}} \Phi_{anis} \ , \tag{3.20}$$

for an anisotropic yield criterion $\Phi_{anis}(\boldsymbol{\Sigma}, q, \mu_w)$. We refer to LUBLINER [1986] for a discussion of the issues behind the derivation of (3.20) given the symmetry restriction $\bar{\boldsymbol{S}} = \bar{\boldsymbol{C}}^{e^{-1}} \boldsymbol{\Sigma} = \boldsymbol{\Sigma}^T \bar{\boldsymbol{C}}^{e^{-1}} = \bar{\boldsymbol{S}}^T$.

3. A poro-visco-plastic model is readily obtained through the so-called Perzyna regularization. The Kuhn-Tucker (3.13) and the consistency (3.14) conditions are replaced by a constitutive law for the consistency parameter γ of the form

$$\gamma = \begin{cases} \frac{1}{\eta_\Phi} \ \mathrm{g}(\Phi, p) \ , & \text{if } \Phi > 0 \\ 0, & \text{otherwise.} \end{cases} \tag{3.21}$$

where $\eta_\Phi > 0$ is a viscous parameter and the regularization function $\mathrm{g}(\Phi, p) : \mathbb{R}_+ \times \mathbb{R} \to \mathbb{R}$ satisfies $\mathrm{g}(\cdot, \cdot) \geq 0$. The simplest choice is given by $\mathrm{g}(\Phi, p) := \frac{1}{2}[\Phi + |\Phi|]$, independent of the pore pressure. □

3.4. A model example: an effective stress model

Consider an elastic potential with the uncoupled form

$$\chi(\bar{\boldsymbol{C}}^e, p, \alpha) = \hat{\psi}_{sk}(\bar{\boldsymbol{C}}^e, \alpha) - b \rho_{w_o} \left(\mu_w(p) - \mu_{w_o}\right) \varepsilon_v^e + \hat{\chi}_{por}(p) \ , \tag{3.22}$$

for a general free-energy ψ_{sk} characterizing the drained response of the solid skeleton and a general function χ_{por}. The common case of a barotropic fluid in terms of the pore pressure field p is considered. In (3.22), we have introduced the notation of ρ_{w_o} for a reference density of the fluid, b for the so-called Biot's coefficient, and

$$\varepsilon_v^e := \log J^e \ , \tag{3.23}$$

for the (logarithmic) elastic volumetric strain with the elastic Jacobian $J^e := \det \boldsymbol{F}^e$.

Given (3.22) and after using equation (3.10), the total stresses read

$$\bar{\boldsymbol{S}} = \bar{\boldsymbol{S}}' - b\rho_{w_o}\,(\mu_w(p) - \mu_{w_o})\,\bar{\boldsymbol{C}}^{e^{-1}} \quad \Longrightarrow \quad \boldsymbol{\tau} = \boldsymbol{\tau}' - b\rho_{w_o}\,(\mu_w(p) - \mu_{w_o})\,\mathbf{1}\,, \tag{3.24}$$

for the *Biot effective stresses*

$$\bar{\boldsymbol{S}}' = 2\partial_{\bar{\boldsymbol{C}}^e}\psi_{sk} \qquad \text{with} \qquad \boldsymbol{\tau}' = \boldsymbol{F}^e\bar{\boldsymbol{S}}'\boldsymbol{F}^{eT}\,, \tag{3.25}$$

given solely in terms of the deformation of the solid skeleton. Considering, for example, the case of an incompressible fluid characterized by

$$\rho_w(p) = \rho_{w_o} \qquad \Longrightarrow \qquad \mu_w = \mu_{w_o} + \frac{p - p_o}{\rho_{w_o}}\,, \tag{3.26}$$

we obtain the relation

$$\boldsymbol{\tau} = \boldsymbol{\tau}' - b\,\vartheta\,\mathbf{1}\,, \qquad \text{for} \qquad \vartheta = p - p_o\,, \tag{3.27}$$

recovering, as usual, the notion of the Terzhagi's effective stress for a unit Biot coefficient $b = 1$; see BIOT [1941].

The potential χ_{por} in (3.22) characterizes the reversible response of the saturated pore space. The simulations presented in Section 4 assume the quadratic potential

$$\hat{\chi}_{por}(p) = -M_o\;(\mu_w(p) - \mu_{w_o}) - \frac{\rho_{w_o}^2}{2\,Q}\,(\mu_w(p) - \mu_{w_o})^2\,, \tag{3.28}$$

for an initial value of the fluid content ($M_o = \rho_{w_o}\phi_{p_o}$ in terms of the initial porosity ϕ_{p_o}) and the (reference) *Biot's modulus* Q. This simple example is appropriate for small changes of the fluid content and results in

$$M^e = M_o + \frac{\rho_{w_o}^2}{Q}\,(\mu_w(p) - \mu_{w_o}) + b\rho_{w_o}\varepsilon_v^e\,, \tag{3.29}$$

leading to a linear relation between the elastic fluid content and the excess pore pressure in the case of an incompressible fluid as given by (3.26).

Similarly, we can consider the common assumption of a yield criterion given in terms of the effective stresses

$$\Phi(\boldsymbol{\tau}, q, \mu_w) = \Phi_{sk}(\tau', q) \le 0\,, \tag{3.30}$$

characterizing the drained plastic response of the solid's skeleton. Isotropy and the case of a barotropic fluid have been assumed in (3.30), without loss of generality. A simple calculation shows that

$$\partial_{\boldsymbol{\tau}}\Phi = \partial_{\boldsymbol{\tau}'}\Phi_{sk} \qquad \text{and} \qquad \partial_{\mu_w}\Phi = -b\rho_{w_o}\partial_{\boldsymbol{\tau}'}\Phi_{sk} : \mathbf{1}\,. \tag{3.31}$$

Then, the plastic evolution $(3.12)_3$ can be written in this case

$$\dot{M}^p = \gamma\, \partial_{\mu_w}\Phi = -b\rho_{w_o}\, \gamma\, \partial_{\boldsymbol{\tau}'}\Phi_{sk} : \mathbf{1} = b\rho_{w_o}\, \tfrac{1}{2}\boldsymbol{\pounds}_{\boldsymbol{v}}\boldsymbol{b}^e\boldsymbol{b}^{e^{-1}} : \mathbf{1}$$

$$= b\rho_{w_o}\boldsymbol{F}^e\, \mathrm{sym}\left[\bar{\boldsymbol{L}}^p\right]\boldsymbol{F}^{eT} : \boldsymbol{b}^{e^{-1}} = b\rho_{w_o}\bar{\boldsymbol{L}}^p : \mathbf{1} = b\rho_{w_o}\, \mathrm{tr}\left[\bar{\boldsymbol{L}}^p\right]\,, \tag{3.32}$$

after using equation (3.7). We further note the relation

$$\mathrm{tr}\left[\bar{\boldsymbol{L}}^p\right] = \dot{\boldsymbol{F}}^p : \boldsymbol{F}^{p^{-T}} = \frac{\dot{J}^p}{J^p} = \dot{\varepsilon}_v^p\,, \qquad \text{where} \quad \varepsilon_v^p := \log J^p\,, \tag{3.33}$$

for the plastic Jacobian $J^p := \det \boldsymbol{F}^p$ and the (logarithmic) plastic volumetric strain ε_v^p, with

$$\varepsilon_v := \log J = \varepsilon_v^e + \varepsilon_v^p\,, \tag{3.34}$$

given the definition (3.23). We then conclude that

$$\dot{M}^p = b\rho_{w_o}\dot{\varepsilon}_v^p\,. \tag{3.35}$$

Equation (3.35) identifies the irreversible change of fluid content with the change of plastic volume (the plastic dilatancy) in the considered effective stress model. We also note the relation

$$\dot{M} = \frac{\rho_{w_o}^2}{Q\ \rho_w}\dot{p} + b\rho_{w_o}\ \dot{\varepsilon}_v\,, \tag{3.36}$$

for the rate of the total fluid content, after combining equations (3.29) and (3.35). In summary, the set of evolution equations (3.12) are then given by

$$\left.\begin{aligned} \boldsymbol{\pounds}_{\boldsymbol{v}}\boldsymbol{b}^e &= -2\gamma\, \partial_{\boldsymbol{\tau}'}\Phi_{sk}\ \boldsymbol{b}^e\,, \\ \dot{\alpha} &= \gamma\, \partial_q\Phi_{sk}\,, \\ \dot{M}^p &= b\rho_{w_o}\dot{\varepsilon}_v^p\,, \end{aligned}\right\} \tag{3.37}$$

for a multiplicative poro-plastic model in effective stresses.

Box 3.1 summarizes the constitutive equations describing the coupled poro-plastic solid for the model example of an elastic response given by Hencky's hyperelastic law of isotropic finite elasticity and a generalized Drucker-Prager yield criterion in effective stresses. A saturation hardening law is assumed. The yield criterion considered in Box 3.1 is of the form (3.15), and thus the resulting constitutive model example conforms with the dissipation inequality (3.18).

Remark 3.3. The above developments, as well as the expressions in Box 3.1, assume a smooth yield surface. Singularities in the yield surface can be treated following the classical approach of KOITER [1953], through the generalized plastic evolution laws

$$\boldsymbol{\pounds}_{\boldsymbol{v}}\boldsymbol{b}^e = -2\left(\sum_\alpha \gamma^{(\alpha)}\boldsymbol{n}_{\Phi}^{(\alpha)}\right)\boldsymbol{b}^e \qquad \text{and} \qquad \dot{\alpha} = \sum_\alpha \gamma^{(\alpha)}\,, \tag{3.38}$$

BOX 3.1. Example: associated poro-plastic model based on Hencky's hyperelastic law and a generalized Drucker-Prager yield criterion in effective stresses.

1. *Elastic stress-strain relations:*

1.1 Drained logarithmic hyperelastic response ($\mu_{sk} > 0$ and $\kappa_{sk} > 0$ constants),

$$\widehat{\Psi}_{sk}(\boldsymbol{b}^e, \alpha) = \tfrac{1}{2}\kappa_{sk} \log^2 J^e + \sum_{A=1,3} \mu_{sk}[\log(\bar{\lambda}^e_A)]^2 + \mathcal{H}(\alpha),$$

where $\bar{\lambda}^e_A = J^{e^{-1/3}} \lambda^e_A$ for the elastic principal stretches λ^e_A (square root of the eigenvalues of $\boldsymbol{b}^e$).

1.2 The Biot effective Kirchhoff stresses are then given by

$$\boldsymbol{\tau}' = 2\boldsymbol{b}^e \partial_{\boldsymbol{b}^e} \Psi_{sk} = \sum_{A=1}^{3} \left[2\mu_{sk} \log \bar{\lambda}^e_A\right] \boldsymbol{n}_A \otimes \boldsymbol{n}_A + \kappa_{sk} J^e \log J^e \mathbf{1}$$

for the spatial principal directions $\boldsymbol{n}_A$ (eigenvectors of $\boldsymbol{b}^e$), with the total stresses given by $(3.24)_2$.

2. *Plastic response:*

2.1 Generalized Drucker-Prager yield criterion

$$\Phi_{sk}(\boldsymbol{\tau}', q) = \frac{1}{\sqrt{2}}\Big(\|\mathrm{dev}[\boldsymbol{\tau}']\| + g(\bar{\tau}')\Big) - [\tau_{yo} - q] \leq 0\,,$$

for $\bar{\tau}' := \mathrm{tr}[\boldsymbol{\tau}']/3$, $\mathrm{dev}[\boldsymbol{\tau}'] := \boldsymbol{\tau}' - \bar{\tau}'\ \mathbf{1}$ $(= \mathrm{dev}[\boldsymbol{\tau}])$, and homogeneous function $g(\cdot)$.

For example, Drucker-Prager's yield criterion is recovered by $g(\bar{\tau}') = \beta_\Phi\ \bar{\tau}'$ with $\tan^{-1}\beta_\Phi =$ angle sustained by Drucker-Prager's cone in the principal stress space.

2.2 Saturation hardening law

$$q := -\partial_\alpha \mathcal{H} = -[H\alpha + (\tau_{yo} - \tau_{y\infty})\ (1 - e^{-\delta_\Phi \alpha})]\,,$$

for constants parameters τ_{yo} (= initial yield limit in shear) , $\tau_{y\infty}$, H and δ_Φ.

2.3 The plastic evolution equations (3.37) read

$$\begin{aligned} \boldsymbol{\pounds}_{\boldsymbol{v}} \boldsymbol{b}^e &= -2\gamma \boldsymbol{n}_\Phi \boldsymbol{b}^e \qquad \text{where} \quad \boldsymbol{n}_\Phi = \frac{1}{\sqrt{2}}\Big(\frac{\mathrm{dev}[\boldsymbol{\tau}']}{\|\mathrm{dev}[\boldsymbol{\tau}']\|} + \tfrac{1}{3} g'(\bar{\tau}')\mathbf{1}\Big)\,, \\ \dot{\alpha} &= \gamma\,, \\ \dot{M}^p &= b\rho_{w_o} \dot{\varepsilon}^p_v = b\rho_{w_o} \frac{\gamma}{\sqrt{2}} g'(\bar{\tau}')\,, \end{aligned}$$

for the derivative $g'(\cdot)$ of $g(\cdot)$, with the loading/unloading and consistency conditions (3.13) and (3.14).

accounting for the outward cone to the yield surface defined by the linear combination $\sum_\alpha \gamma^{(\alpha)} \boldsymbol{n}_{\Phi}^{(\alpha)}$. Equivalently, approaches based on convex analysis can be found in MOREAU [1976], among others. For the simple case of a Drucker-Prager model consisting of a cone in the principal (effective) stress space, with a vertex on the hydrostatic axis at τ'_{vertex}, the flow rule reads

$$\boldsymbol{\pounds}_{\boldsymbol{v}} \boldsymbol{b}^e = -\sqrt{2} \left[\gamma^{(1)} \left(\frac{\mathrm{dev}[\boldsymbol{\tau}']}{\|\mathrm{dev}[\boldsymbol{\tau}']\|} + \tfrac{1}{3}\beta_{\Phi} \mathbf{1} \right) + \gamma^{(2)} \, \tfrac{1}{3}\beta_{\Phi} \, \mathbf{1} \right] \boldsymbol{b}^e \, , \tag{3.39}$$

with $\beta_{\Phi} = g'(\bar{\tau}'_{vertex})$ and the plastic multiplier $\gamma^{(2)}$ imposing the constraint $g(\bar{\tau}') \leq g(\bar{\tau}'_{vertex})$ for the compressive cone of the yield surface ($\gamma^{(2)} = 0$ except in the vertex). □

3.5. An a-priori stability estimate for multiplicative poro-plasticity

The equations summarized in Section 2, together with the multiplicative poro-plastic model presented in the previous sections, define a dissipative abstract problem of evolution. To characterize this dissipative structure, we consider in the quasi-static case of interest the functional

$$\boxed{\mathcal{L}(\boldsymbol{\varphi}, p; \mathcal{I}) := \int_{\mathcal{B}} \Big[\underbrace{\chi(\boldsymbol{\varphi}, p\,; \mathcal{I}) + \mu_w(p)\; M^e(p, \mathcal{I})}_{\hat{\psi}(\boldsymbol{\varphi}, M^e(p,\mathcal{I})\,; \mathcal{I})} - \mu_{w_o} M(\boldsymbol{\varphi}, p; \mathcal{I}) \Big] \, dV \, ,} \tag{3.40}$$

for the constant reference value of the chemical potential of the fluid μ_{w_o}. In (3.40), we have used the potential χ to emphasize the role of the pore pressure field p as primary variable rather than the fluid content. As discussed in the Appendix, the finite element methods employed in the solution of the problem consider the interpolation of the this field p.

Consider equations (2.8) under the assumptions of no body forces and boundary tractions (2.24)

$$\boldsymbol{f} = \mathbf{0} \quad \text{in} \quad \mathcal{B} \quad (\text{i.e. } \mathcal{V}_{ext} = 0) \qquad \text{and} \qquad \boldsymbol{P}\boldsymbol{N} = \mathbf{0} \quad \text{on} \quad \partial_T \mathcal{B} \, , \tag{3.41}$$

and constant in time essential boundary conditions $\bar{\boldsymbol{\varphi}}(\boldsymbol{X})$ in $\partial_{\boldsymbol{\varphi}}\mathcal{B}$. The evolution of the functional $\mathcal{L}$ along the solutions of the problem under these conditions is given by

$$\begin{aligned} \frac{d\mathcal{L}}{dt} &= \int_{\mathcal{B}} \left[\dot{\psi} - \mu_{w_o} \dot{M} \right] dV = \int_{\mathcal{B}} \Big[\underbrace{\boldsymbol{\tau} : \boldsymbol{d} + \mu_w \dot{M} - \mathcal{D}_{int}}_{\dot{\psi} \text{ by (2.18)}} - \mu_{w_o} \dot{M} \Big] \, dV \\ &= - \int_{\mathcal{B}} \Big[\underbrace{\mathcal{D}_{cond} + \mathcal{D}_{int}}_{\substack{\mathcal{D} \geq 0 \\ \text{by (2.16)}}} \Big] \, dV + \int_{\partial\mathcal{B}} (\mu_{w_o} - \mu_w) \, \boldsymbol{Q}_w \cdot \boldsymbol{N} \, dA \\ &\leq \int_{\partial\mathcal{B}} (\mu_{w_o} - \mu_w) \, \boldsymbol{Q}_w \cdot \boldsymbol{N} \, dA \, . \end{aligned} \tag{3.42}$$

We conclude that

$$\text{IF} \quad (\mu_{w_o} - \mu_w)\, \boldsymbol{Q}_w \cdot \boldsymbol{N} \leq 0 \quad (\Longleftrightarrow \ (\mu_{w_o} - \mu_w)\, \boldsymbol{q}_w \cdot \boldsymbol{n} \leq 0) \quad \text{on} \quad \partial\mathcal{B} \tag{3.43}$$

$$\Longrightarrow \quad \boxed{\frac{d\mathcal{L}}{dt} \leq 0\,,} \tag{3.44}$$

that is, the functional $\mathcal{L}$ decreases along the flow defined by the solutions of the problem if the fluid boundary conditions satisfy (3.43). This condition is satisfied by a general boundary condition of the form

$$\boldsymbol{Q}_w \cdot \boldsymbol{N} = -\kappa_s \ (\mu_{w_o} - \mu_w) \ , \tag{3.45}$$

for a non-negative surface permeability coefficient $\kappa_s \geq 0$. In particular, impervious ($\boldsymbol{Q}_w \cdot \boldsymbol{N} = 0$) and free drainage ($\mu_w = \mu_{w_o}$) boundary conditions satisfy condition (3.43).

The functional $\mathcal{L}$ can be recognized as the analog of the a-priori stability estimate developed in ARMERO & SIMO [1993] for the analog system of multiplicative thermoplasticity, an analogy usually referred to as Biot's analogy (BIOT [1956b]). The analogy follows formally with the identification of p with the temperature field, Ψ_{sk} with the isothermal free energy of the solid, $1/Q \to \bar{c}$ with the heat capacity, $\boldsymbol{k}$ with the thermal conductivity tensor, and $b \to 3\kappa_{iso}\alpha_T$ in terms of the isothermal bulk modulus κ_{iso} and the linear coefficient of thermal expansion α_T. The analogy is completed by identifying the fluid content field M with the entropy of the thermoelastic solid.

In the case of finite strain thermoelastic theories, the functional $\mathcal{L}$ corresponds to the analog of the so-called *canonical free energy* as originally considered in DUHEM [1911]. For the linearized problem of thermoelasticity, it was shown in DAFERMOS [1976] that $\mathcal{L}$ defines a Lyapunov functional under the classical assumption of positive definite tangent moduli. Complete analyses identifying the conditions for $\mathcal{L}$ to define a Lyapunov functional for the finite strain thermoelastic problem can be found in ERICKSEN [1966], COLEMAN & DILL [1973], GURTIN [1975], and BALL & KNOWLES [1986]. In the coupled fluid-solid system of interest herein, the decay of the functional $\mathcal{L}$ is related to the stability of the stress free-state of the porous solid, as imposed by (3.41), and ambient constant reference chemical potential μ_{w_o} for the fluid. In this setting, the estimate (3.42) can be found in COUSSY [1995] (page 108) for the case of poro-elasticity. The result (3.42) shows the applicability of this estimate to the proposed multiplicative finite strain poro-plastic model.

It is important to emphasize that the stability of the solution follows rigorously only for poro-elasticity under the proper conditions of the material parameters leading to a convex free energy function. In the general case of finite deformation poro-plasticity, this result does not apply since $\mathcal{L}$ does not define a convex function (a norm) of the primary fields $\{\varphi, p; \mathcal{I}\}$, so material instabilities are not precluded by the estimate (3.44). The situation occurs also in infinitesimal theories of perfect and softening plasticity. Non-smooth solutions involving highly localized patterns of the deformation and, in fact, the

BOX 3.2. Two operator splits for the coupled poro-plastic problem in the quasi-static range.

THE DRAINED SPLIT

Problem 1. (Drained Solid Phase)	**Problem 2.** (Fluid Phase)
$\text{DIV}\,\boldsymbol{P} + \rho_o \boldsymbol{f} = 0$ $c\dot{p} = 0$	$\dot{\varphi} = 0$ $c\dot{p} = -\,\text{DIV}\,\boldsymbol{Q}_w + \mathcal{S}^{ep}$

where $c := -\dfrac{\partial}{\partial p}\left[\rho_w \dfrac{\partial \chi}{\partial p}\right]$, and $\mathcal{S}^{ep} := \rho_w \dfrac{\partial^2 \chi}{\partial \bar{\boldsymbol{C}}^e \partial p} : \dot{\bar{\boldsymbol{C}}}^e + \rho_w \dfrac{\partial^2 \chi}{\partial \alpha \partial p}\dot{\alpha} - \dot{M}^p$.

THE UNDRAINED SPLIT

Problem 1. (Undrained Solid Phase)	**Problem 2.** (Fluid Phase)
$\text{DIV}\,\boldsymbol{P} + \rho_o \boldsymbol{f} = 0$ $\dot{M} = 0$	$\dot{\varphi} = 0$ $\dot{M} = -\,\text{DIV}\,\boldsymbol{Q}_w$

limit case of strong discontinuities, with the associated singular strain fields, are observed preceding the failure of the solid. We refer to ARMERO & CALLARI [1998] for a recent analysis of these solutions in the coupled poro-plastic framework described herein, together with the development of numerical tools for their simulation. However, the inequality (3.44) still furnishes an *a-priori stability estimate* to be inherited by the solutions obtained by the numerical algorithms approximating the exact flow, as discussed briefly in the following remark.

Remark 3.4. Given the aforementioned analogy with thermomechanical problems, the results presented in ARMERO & SIMO [1992,93] in the context of coupled thermo-elasto-plasticity apply to this case, identifying the stable partitions of the coupled problem and associated staggered algorithms. In particular, the analog of the so-called adiabatic split, as developed in these references, has its counterpart in the coupled solid/fluid system of interest herein in the partition of the problem in a mechanical solid phase involving the solution of the equilibrium equation (2.8) at fixed fluid content M, followed by a fluid phase corresponding to the dissipation of the excess pore-pressure through Darcy's law with the solution of (2.7). We refer to this operator split of the problem as the *undrained split,* in contrast with the *drained split* consisting of an initial solid phase at fixed pore pressure. See Box 3.2 for an illustration of these ideas. In particular, a simple calculation

following (3.42) leads to

$$\left.\frac{d\mathcal{L}}{dt}\right|_{\substack{\dot{p}=0 \\ \text{(drained)}}} = -\int_{\mathcal{B}} \mathcal{D}_{int}\, dV + \underbrace{\int_{\partial\mathcal{B}} (\mu_{w_o} - \mu_w)\, \dot{M}\, dA}_{\lesseqgtr 0,\ \text{in general}}\,, \tag{3.46}$$

$$\left.\frac{d\mathcal{L}}{dt}\right|_{\substack{\dot{M}=0 \\ \text{(undrained)}}} = -\int_{\mathcal{B}} \mathcal{D}_{int}\, dV \leq 0\,, \tag{3.47}$$

showing that the undrained split conforms with the dissipative character of the problem of evolution by inheriting each phase of the partition the a-priori stability estimate (3.42) of the exact coupled problem, in contrast with the drained split of the problem. The numerical stability of the time-stepping schemes based on the undrained split, with each sub-problem solved with a stable scheme (in the sense that (3.42) is preserved), is then concluded *in the general fully nonlinear finite strain coupled poro-plastic range.* We refer again to ARMERO & SIMO [1992,93] for full details of the analyses and to the Appendix I for details in the numerical implementation for the problem of interest herein. In the context of consolidation problems, staggered algorithms based on a drained solid phase can be found in PARK [1983] or LEWIS & SCHREFLER [1987], among many others, and on an undrained solid phase in ZIENKIEWICZ et al [1988] for the linear elastic consolidation problem. □

4. Representative Numerical Simulations

The goal of this section is to assess numerically the finite strain poro-plastic framework developed in this work. To this purpose, we present the results obtained with the proposed formulation for two characteristic benchmark problems. Section 4.1 considers the finite elastoplastic consolidation of a porous layer under the action of a rigid footing. The analysis of strain localization in the plane strain compression test under globally undrained conditions is considered in Section 4.2.

The constitutive models and numerical algorithms described in the previous sections have been implemented in the finite element code FEAP (see ZIENKIEWICZ & TAYLOR [1991]). In all the finite element simulations reported in this section, we make use of the Q1/ET4 enhanced strain quadrilateral finite element presented in GLASER & ARMERO [1997]. We note the need for the use of these improved elements in the solution of the problems of interest herein. Even though the plastic flow given by the considered Drucker-type models leads to a dilatant response, in contrast with typical applications in metal plasticity, the quasi-incompressible nature of the problem can be traced back to the coupling of the (quasi-) incompressible fluid. In particular, the quasi-incompressible character

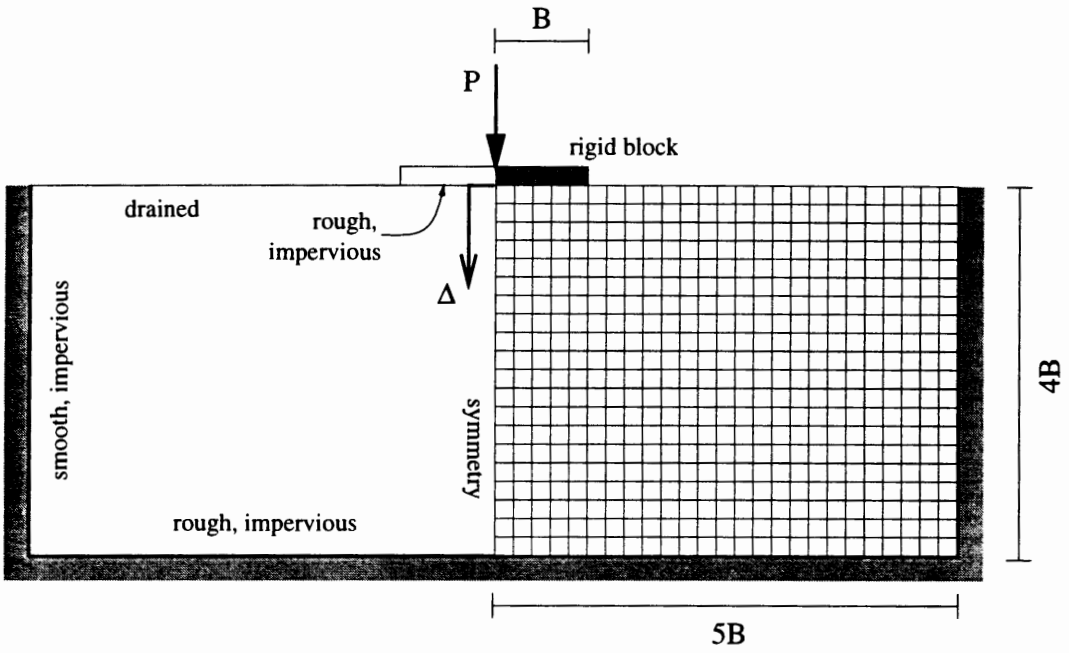

FIGURE 4.1. Finite strain consolidation. Problem definition with assumed boundary conditions, and finite element discretization of half of the specimen by symmetry (structured 25 × 20 mesh of Q1/ET4 enhanced quads).

of the undrained elasticities for typical large values of the Biot modulus Q is to be noted; see the Appendix I. Furthermore, the implementation of the pressure dependent coupled poro-plastic model developed in Section 3 becomes straightforward in the fully strain-driven structure of this class of finite elements. This fact, together with the modular structure of the considered staggered schemes, leads to a numerical implementation involving simple modifications of existing program modules. We refer to the Appendix I for further details regarding different aspects of the numerical implementation.

4.1. Finite strain elastic and elastoplastic consolidation

This section presents the results for a finite elastic and elastoplastic consolidation problem. We consider the benchmark test presented in CARTER et al [1979]. The problem consists of a rigid rectangular footing $2 \times B$ wide resting on a layer of saturated soil $2 \times 5B$ wide by $4B$ deep. The value of $B = 1\ m$ has been considered in the actual numerical simulations. This layer sits on a rigid rough base and it is confined by two rigid smooth walls. Plane strain conditions are assumed. Figure 4.1 depicts the geometry and boundary conditions considered in the problem. In particular, the top free boundary of the porous layer is supposed to allow the drainage of the specimen. The contact surface with the rigid footing is assumed impervious and rough (that is, stick boundary conditions are imposed). Due to symmetry considerations, only the right half of the specimen is discretized, with a

TABLE 4.1. Finite strain consolidation. Material properties.

Bulk Modulus	κ_{sk}	212.33	MPa
Shear Modulus	μ_{sk}	98.0	MPa
Initial Yield Limit in Shear	τ_{yo}	17.32	MPa
Saturation Yield Limit in Shear	$\tau_{y\infty}$	23.10	MPa
Saturation Hardening Parameter	δ_Φ	0.20	
Pressure Yield Parameter	β_Φ	0.10	
Fluid Density	ρ_{w_o}	1000.0	Kg/m^3
Biot Modulus	Q	511.0	MPa
Biot coefficient	b	1.0	
Hydraulic Permeability	k_{h_o}	$2.07 \cdot 10^{-3}$	m/s

structured mesh consisting of 25×20 Q1/ET4 enhanced strain quads. Similarly, the right half of the rigid block is modeled with equal 5×1 quads.

The two cases of a finite elastic and finite elastoplastic porous layer are considered. For the finite poro-elasto-plastic layer, the associated Drucker-Prager model described in Section 3.4 and summarized in Box 3.1 is considered. Table 4.1 includes the material properties assumed in the simulations reported herein. In particular, a saturation law is considered for the hardening response of the solid skeleton. The fluid is assumed to have the constant density ρ_{w_o}. The finite elastic case is recovered by simply considering high yield limits τ_{yo} and $\tau_{y\infty}$, so yielding does not occur. The rest of the material parameters are assumed the same. The final model consists then of a Hencky hyperelastic law together with the fluid coupling characterized by relation (3.29). The rigid footing is modeled with five finite elements having very large elastic constants compare to the corresponding values in the layer. Gravity effects are neglected.

The specimen is loaded with a load P, applied rapidly at the center of the rigid footing. The final value of $P/(B\mu_{sk}) = 2.5$ is considered in all the reported solutions. The layer is then left to consolidate in time. The analysis of one-dimensional consolidation in the infinitesimal range presented in BIOT [1941] identifies the *consolidation constant*

$$\frac{1}{c_v} = \frac{\gamma_{w_o}}{k_{h_o}} \left(b^2 \, \frac{(1+\nu_{sk})}{3\kappa_{sk}(1-\nu_{sk})} + \frac{1}{Q} \right) , \tag{4.1}$$

for the Poisson ratio of the solid skeleton $\nu_{sk} = (3\kappa_{sk} - 2\mu_{sk})/[2(\kappa_{sk} + \mu_{sk})]$. As it is customary in the literature, we report the results below in terms of the non-dimensional time

$$T := \frac{c_v \, t}{(4 \, B)^2} , \tag{4.2}$$

for the assumed depth of the layer $4B$.

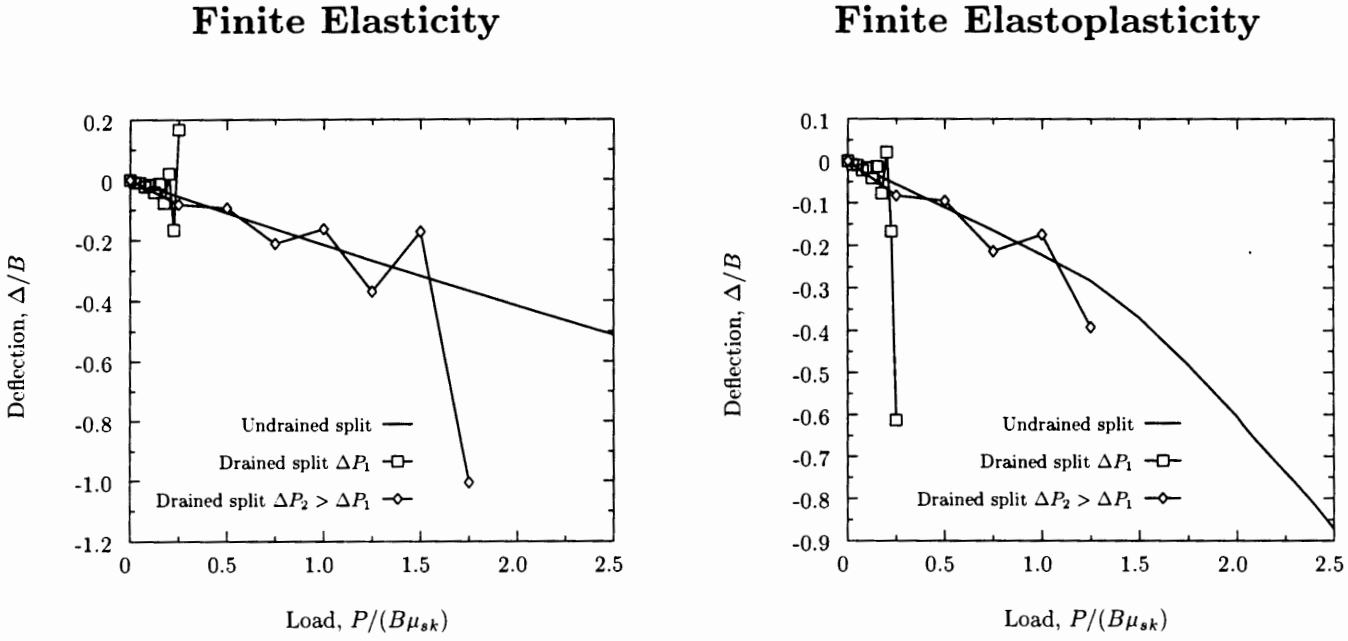

FIGURE 4.2. Finite strain consolidation. Evolution of the deflection under the block Δ/B with the imposed load $P/(B\mu_{sk})$ (final non-dimensional time $T = 2.65 \cdot 10^{-6}$ at $P_{final}/(B\mu_{sk}) = 2.5$) for the elastic and elastoplastic solutions, and different schemes. The instability of the drained split as the load increment decreases is apparent ($\Delta P_1 = 10\Delta P_2 = P_{final}/10$).

To model a suddenly applied load, the load P is increased linearly from $T = 0$ to its final value of $P/(B\mu_{sk}) = 2.5$ at $T = 2.65 \cdot 10^{-6}$. Figure 4.2 shows the load-deflection curves obtained for the finite elastic and finite elastoplastic cases. The simulations are run with the staggered schemes based on the undrained and drained split of the equations, and the block Gauss-Seidel iteration scheme described in the Appendix I. As we can observe in this figure, the scheme based on the undrained split is able to obtain the solution along this sudden increase of the load. The solutions reported in Figure 4.2 were obtained with a total of 20 time steps. In contrast, we can observe the instability inherent to the scheme based on the drained split, as identified in Section 3.5. We obtain an uncontrollable growth in time of the solution, which becomes worse as the time step (or, equivalently, the load step) decreases. The solutions depicted in Figure 4.2 use load increments of $\Delta P_1 = 10\Delta P_2 = P_{final}/10$. The same instabilities are obtained when trying to converge the block Gauss-Seidel scheme. This response is consistent with the results presented in ARMERO & SIMO [1992] who identified in the analog context of thermoelasticity the stability conditions of the type $\Delta t/h^2 > constant$ for the convergence of these schemes in the quasi-static case. We refer also to TURSKA & SCHREFLER [1993] who reported similar experiences. Given this stringent stability restrictions, we have not been able to

Finite Elasticity:

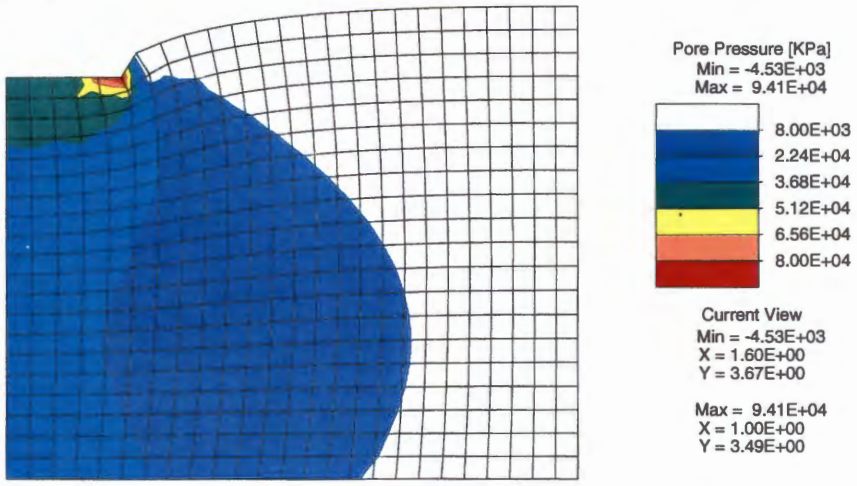

Finite Elastoplasticity:

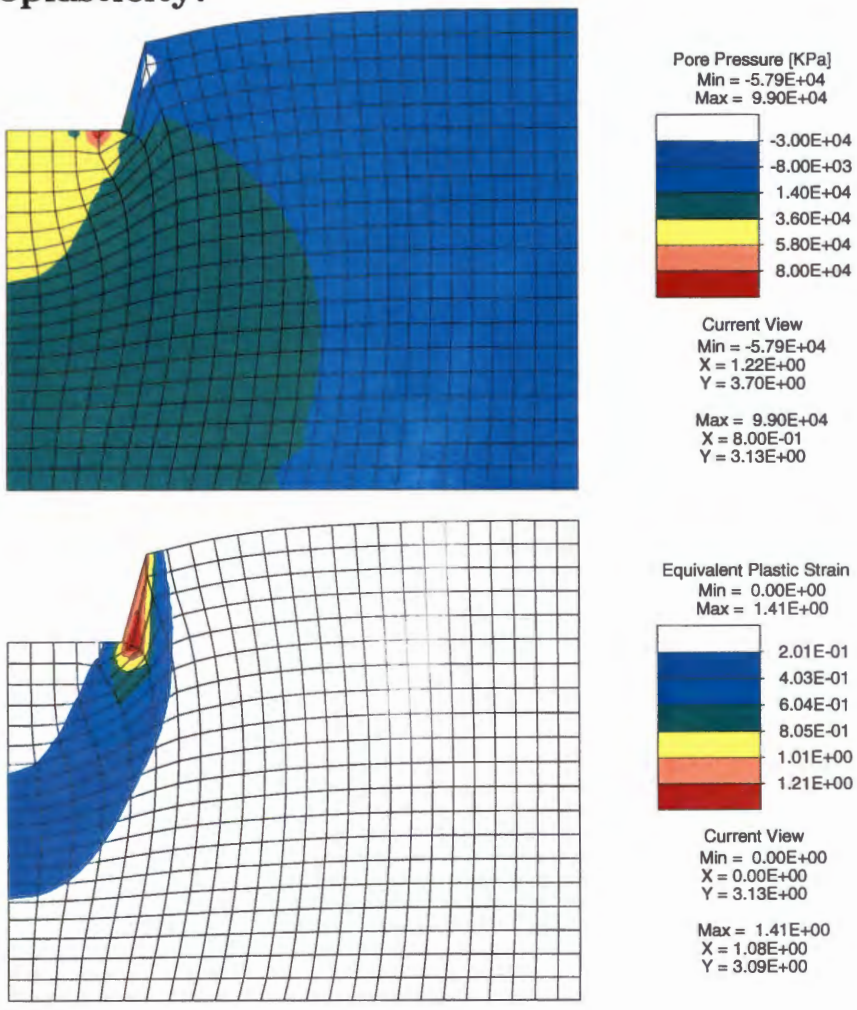

FIGURE 4.3. Finite strain consolidation. Distribution of the pore pressure p at $P/(B\mu_{sk}) = 2.5$ ($T = 2.65 \cdot 10^{-6}$) for the elastic and elastoplastic solutions, and of the equivalent plastic strain for the elastoplastic solution (no magnification of the deformations).

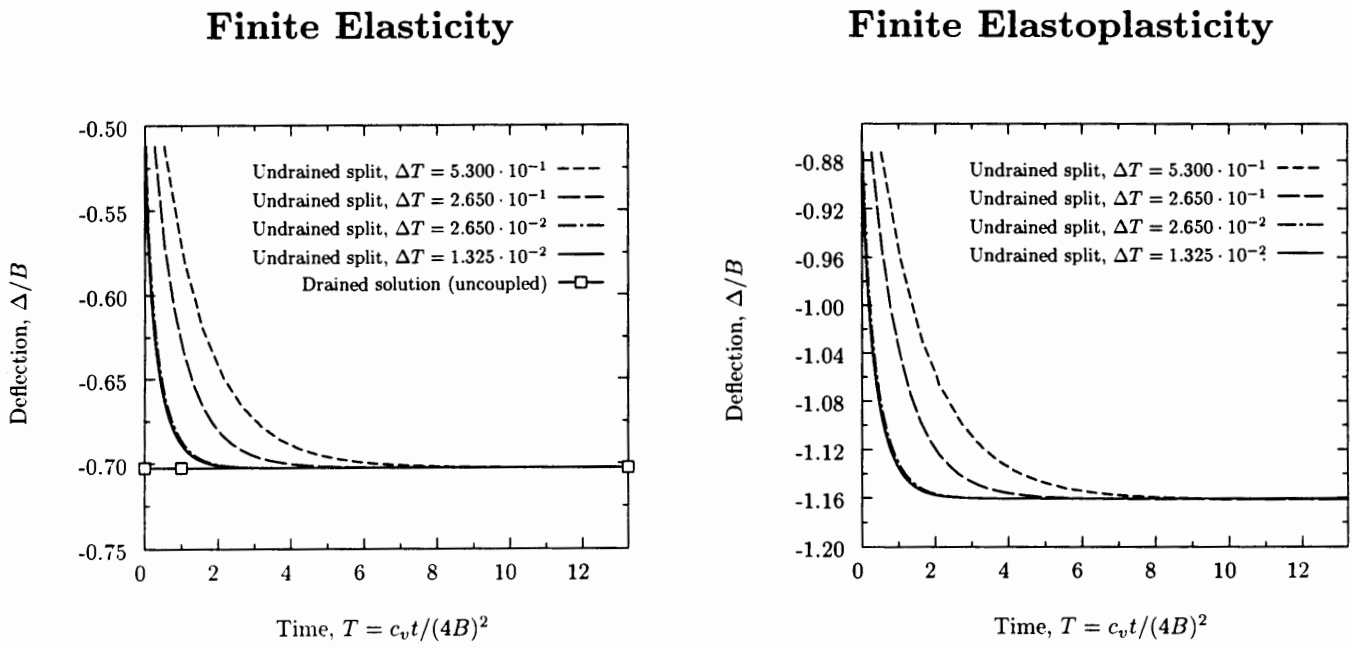

FIGURE 4.4. Finite strain consolidation. Evolution of the deflection under the block Δ/B with time for the elastic and elastoplastic solutions, and different time steps. Note the difference in the vertical scales.

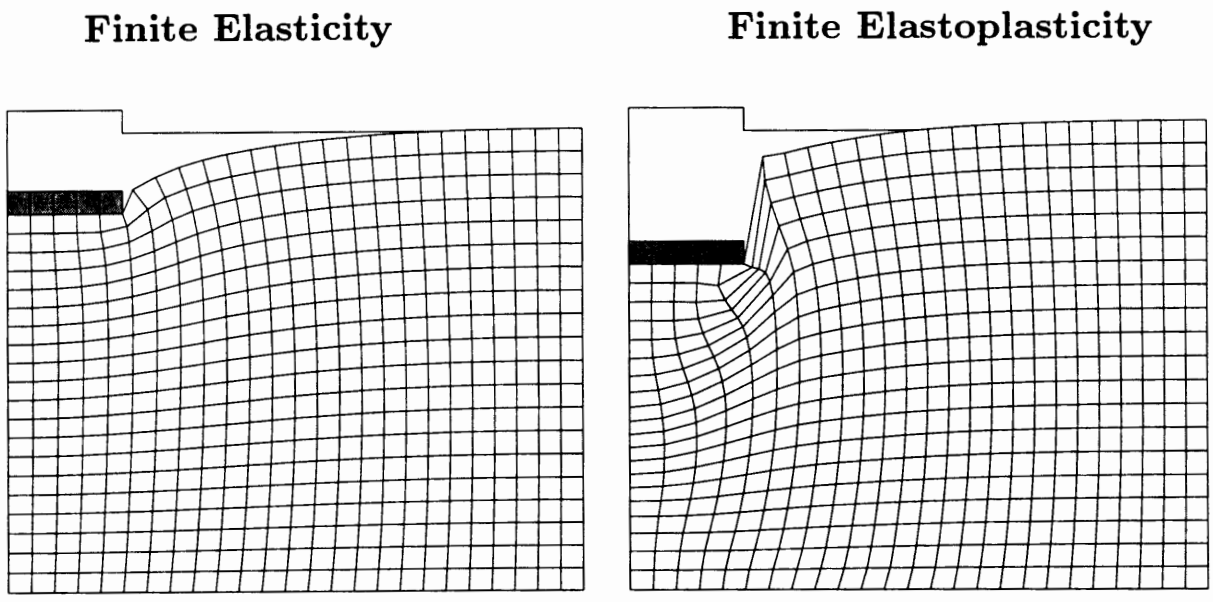

FIGURE 4.5. Finite strain consolidation. Deformed configuration at $T = 13.25$ for the elastic and elastoplastic solutions (obtained with $\Delta T = 2.65 \cdot 10^{-2}$, no magnification of the deformations).

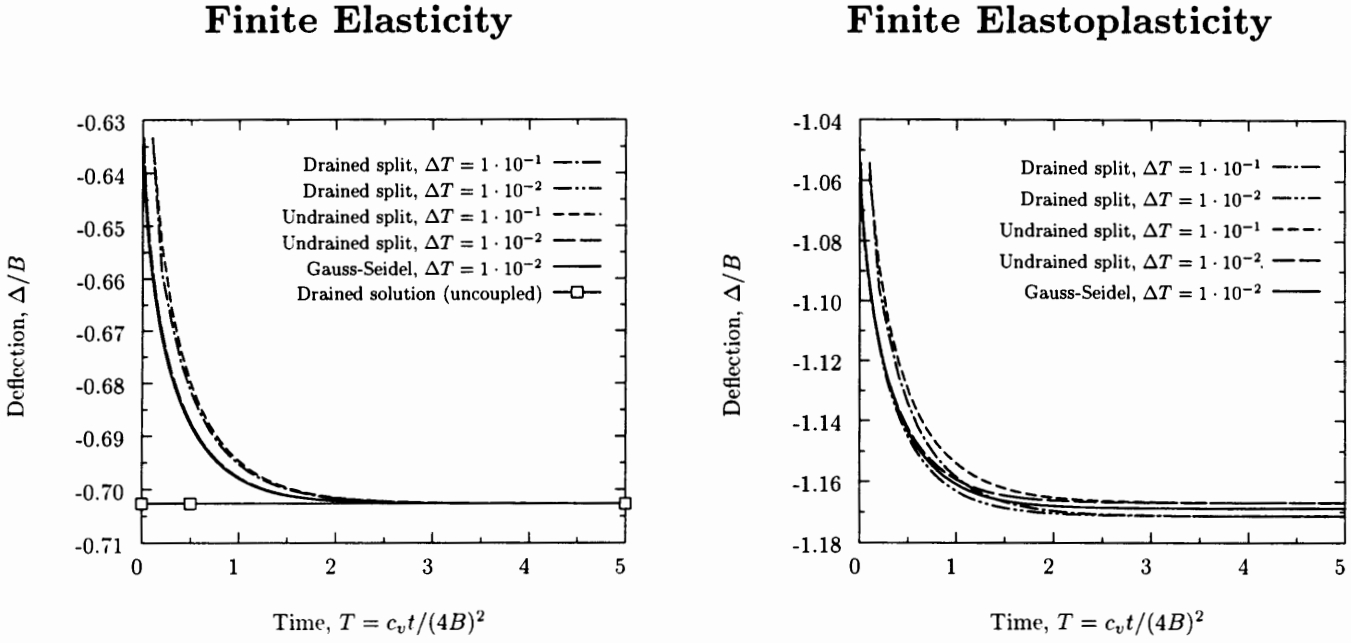

FIGURE 4.6. Finite strain consolidation. Evolution of the deflection under the block Δ/B with time for the elastic and elastoplastic solutions, and different time steps for low Biot modulus $Q = 100\ MPa$ (note the difference in the vertical scales).

solve these early stages of the sudden imposition of the load with the schemes based on a drained mechanical problem for the given mesh. Extremely fine meshes would be required.

This situation is to be contrasted with schemes based on the undrained split. The solution at this initial stage ($T = 2.65 \cdot 10^{-6}$) has been depicted in Figure 4.3. We have included the distribution of the pore pressure in both the elastic and elastoplastic solutions, as well as the equivalent plastic strain α in the elastoplastic solutions, all of them superimposed over the deformed configuration of the solid. The different patterns of the deformation between the elastic and the softer inelastic case are to be noted. In particular, we observe that the appearance of the plastic zone leads to a decrease of the pore pressure due to the plastic dilatancy predicted by the poro-plastic model under consideration. The process is essentially undrained given the high rate of loading. In contrast, the excess pore pressure exhibits a more smooth distribution in the finite elastic case. We note that the reference (back) pressure of $p_o = 0$ has been used in reporting the values in Figure 4.3.

The layer is left to consolidate thereafter. Figure 4.4 includes the evolution of the vertical deflection under the rigid footing (Δ/B) as a function of the non-dimensional time T. Both the elastic and elastoplastic solutions are included. We note, in this respect, the different scales of the deflection, including the different initial and final settlement. The characteristic parabolic-type curve predicted by Biot's theory is obtained; see BIOT

[1941] for details in the infinitesimal linear elastic case. We have included in Figure 4.5 the deformations obtained in the finite elastic and the finite elastoplastic simulations at the consolidated state of $T = 13.25$, side by side for comparison. The softer response of the elastoplastic solution is apparent.

Figure 4.4 reports the results obtained in simulations with different values of the time step, with values ranging between $\Delta T = 5.30 \cdot 10^{-1}$ to $\Delta T = 1.325 \cdot 10^{-2}$. Equal time increments are considered in a given simulation. All the simulations involve the undrained split since, as noted above, no convergence was obtained with the drained split nor the Gauss-Seidel schemes. For the finite elastic case, we have included the solution obtained with an uncoupled drained simulation of the problem, which corresponds in the elastic case with the final steady state solution. This situation is to be contrasted with the path dependent elastoplastic case under consideration. Figure 4.4 show a good agreement in the long term, in particular, with the steady state limit solution in the elastic case. We can also observe, however, that the discrepancy of the different solutions in early stages is larger, specially in the elastoplastic (path-dependent) case. This is an indication of the numerical error associated to the scheme in the strongly coupled case. We recall that the considered staggered schemes are only first order accurate in time due to the error associated with the partition, regardless of the temporal accuracy of the algorithm employed in each individual sub-problem. This feature, although undesirable, needs to be pondered with the stability of the scheme based on the undrained split. No instabilities in time (that is, uncontrollable growth of the solution) have been observed in the numerical experiments with this scheme.

We have included in Figure 4.6 the results obtained with a lower Biot modulus of $Q = 100\ MPa$, all other parameters equal. In this less realistic case, the schemes based on the drained split do not show instabilities for the time steps considered. We have included also the solution obtained with a very small time step ($\Delta T = 1 \cdot 10^{-2}$) in combination with the Gauss-Seidel iteration to convergence at each time step, obtaining effectively in this way the fully coupled solution of the monolithic scheme. We note that a typical time increment of this Gauss-Seidel scheme may take up to 40 passes (each pass involving the solution of the two phases), to be compared in computational cost with the single-pass undrained or drained staggered schemes. A good agreement is observed for the elastic case between the different schemes and same time steps. We observe different steady state solutions in the elastoplastic path-dependent case. As expected, the undrained and drained splits lead to a stiffer and softer solutions, respectively, when compared to the fully coupled solution. The same order of accuracy can be observed for these staggered schemes in this case. Both are first order accurate as noted above.

4.2. The plane strain compression test

We report in this section the results obtained for the plane strain compression test under globally undrained conditions. This test has become a classical benchmark problem

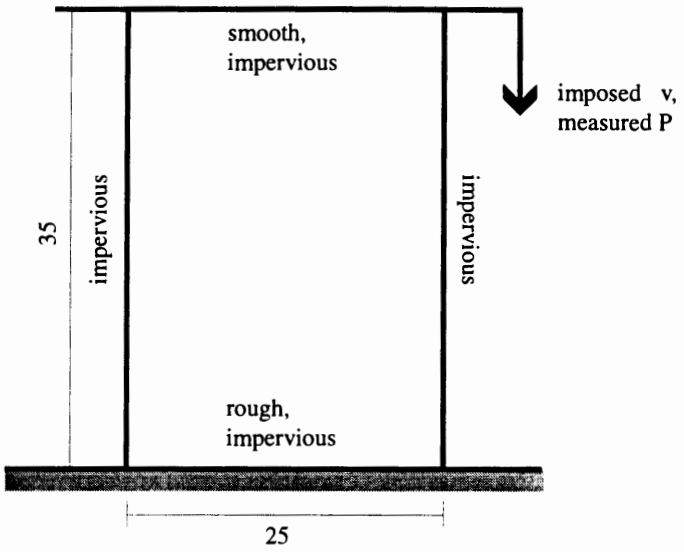

FIGURE 4.7. Plane strain compression test. Configuration of the problem with the assumed boundary conditions. Due to the symmetry, only the right half of the specimen is modeled with 10 × 24 Q1/ET4 enhanced strain finite elements.

for the numerical study of strain localization under coupled fluid flow conditions. We refer to the analytical study of the problem presented in VARDOULAKIS [1996a,b], and to LORET & PREVOST [1991] and SCHREFLER et al [1995,97] for representative finite element studies of this test, the last one involving a partially saturated model. To our knowledge, all the results reported in the literature to the present involve the infinitesimal range.

For the case of study herein, we consider the same specimen studied in SCHREFLER et al [1997], consisting of a rectangular block of dimensions $H = 35\ cm$ and $W = 25\ cm$. Figure 4.7 depicts the block under consideration with the assumed boundary conditions. All the boundaries are assumed impervious, in order to study the formation of shear bands under globally undrained conditions. Stick conditions in the displacement are assumed at the bottom boundary, whereas an uniform vertical displacement $\bar{v}$ is imposed at the top boundary with the specimen free too move laterally. Gravity effects are neglected.

The isotropic Drucker-Prager model described in Section 3.4, and summarized in Box 3.1, is considered in the simulations. The assumed material properties are included in Table 4.2. In particular, we note the consideration of linear strain softening to trigger the formation of the localized solutions. To study the effect of the solid's permeability, two different values of the hydraulic permeability (see Remark 2.1.1) are considered, namely, $k_{h_o} = 5 \cdot 10^{-9}\ m/s$ and $k_{h_o} = 1 \cdot 10^{-22}\ m/s$, with the last one recovering effectively the fully undrained case.

An fluid response characterized by a constant density $\rho_w = \rho_{w_o}$, as in (3.26), is assumed. We note that cavitation effects has been observed in similar experimental tests;

TABLE 4.2. Plane strain compression test. Material properties.

Bulk Modulus	κ_{sk}	250.0	MPa
Shear Modulus	μ_{sk}	100.0	MPa
Yield Limit in Shear	τ_{yo}	5.77	MPa
Softening Modulus	H	-4.62	MPa
Pressure Yield Param.	β_Φ	0.2	
Fluid Density	ρ_{w_o}	1000.0	Kg/m^3
Biot Modulus	Q	511.0	MPa
Biot coefficient	b	1.0	

see SCHREFLER et al [1997] and references therein. We consider in this first study at the finite strain range the simplying assumption of an incompressible fluid. A high value of the back pressure $p_o = 29\ MPa$ has been considered when reporting the pore pressure values below. We note also that a uniform reference fluid content of $M_o = 200\ kg/m^3$, corresponding to an initial porosity of $\phi_{p_o} = 0.2$ (with $M_o = \phi_{p_o}\rho_{w_o}$), has been considered in depicting the results below.

Due to the symmetry in the problem, only the right half of the specimen is considered in the numerical simulations, with the corresponding symmetry boundary conditions at the center. The simulations are carried out under displacement control of the imposed vertical deflection of the top surface $\bar{v}$, with the measurement of the corresponding reacting force R. Quasi-static conditions are assumed, that is, neglecting the transient term in the solid's mechanical equation while maintaining the rate term in the equation of conservation of fluid mass. A nominal strain rate of $\dot{\bar{v}}/H = 2.86 \cdot 10^{-3}\ s^{-1}$ is considered. We use the algorithm based on the *undrained split*, consisting of an undrained solid problem solved at the end of the time step t_{n+1}, followed by the fluid phase problem, solved with the backward-Euler scheme. See Appendix I for complete details.

A regular mesh of 10×24 quadrilateral finite elements is considered, with the Q1/ET4 enhanced strain finite elements presented in GLASER & ARMERO [1997]. We note that, in this case, the need for these improved finite elements arises not only from the quasi-incompressibility constraint added by the coupling of the incompressible fluid, but also the need of finite elements capable of resolving the localized patterns of the deformation observed in the final solutions. These elements have been shown to exhibit these properties, with the added advantage of possessing a completely strain driven structure; see this last reference. We also note that it is not our intention in this paper to study the possible mesh-dependence of the solutions due to the presence of the strain-softening. We refer to ARMERO & CALLARI [1998] for a discussion of these issues in the coupled framework described herein for the infinitesimal range.

Figures 4.8 and 4.9 depict the solutions obtained for the higher permeability case. We have included the distribution of the pore pressure p, fluid content M, equivalent plastic

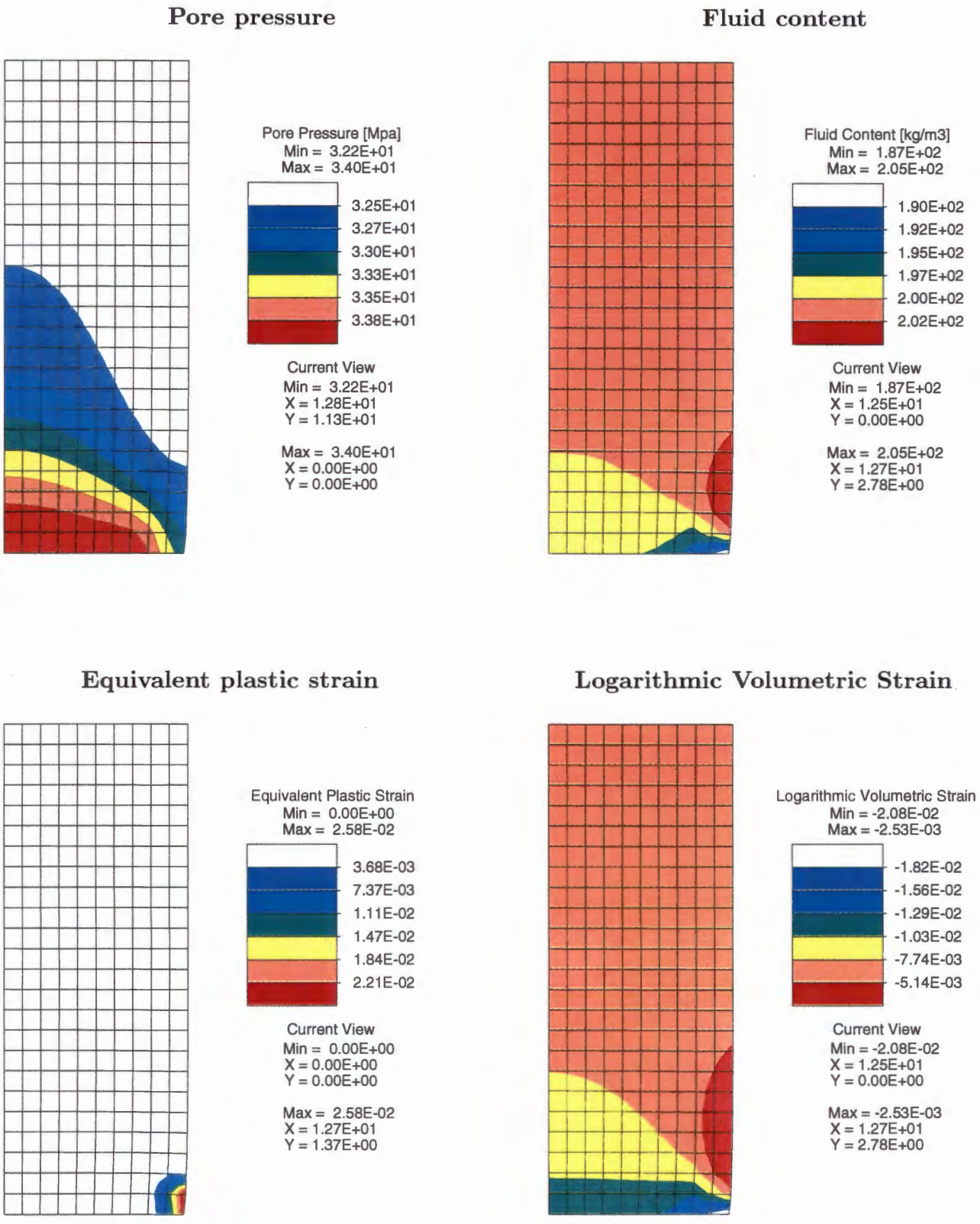

FIGURE 4.8. Plane strain compression test. Solutions at an imposed top vertical displacement of $\bar{v} = 1.0\ cm$ ($k_{h_o} = 5 \cdot 10^{-9}\ m/s$; no magnification of the deformations).

Pore pressure

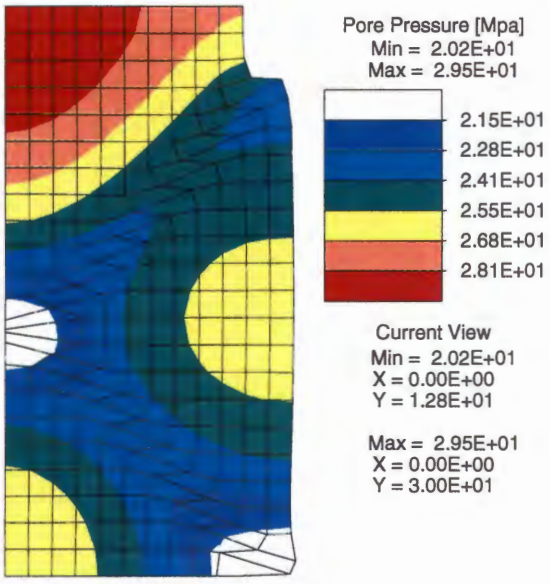

Fluid content

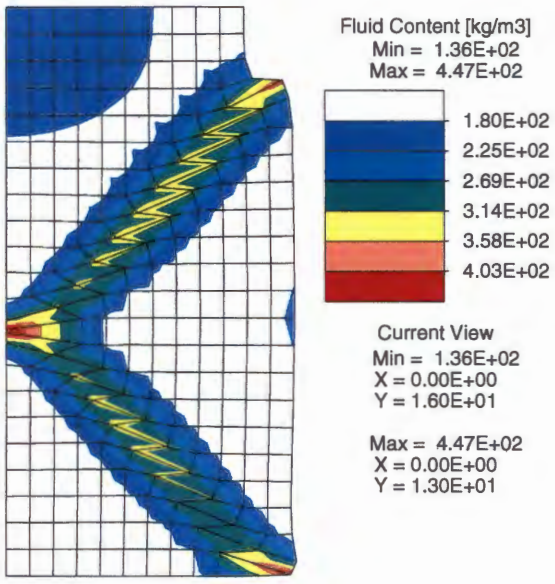

Equivalent plastic strain

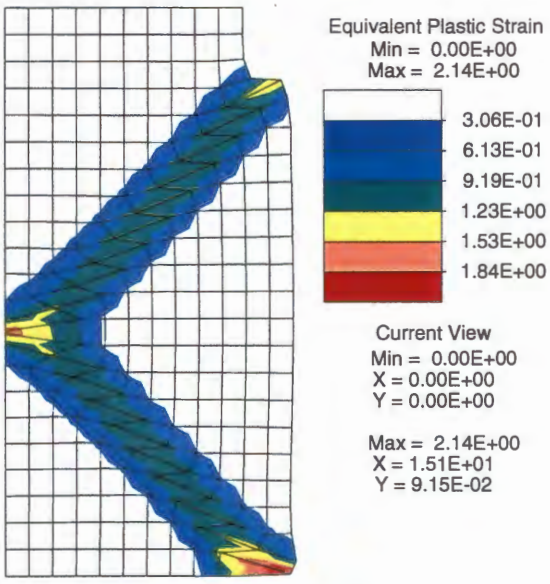

Logarithmic Volumetric Strain

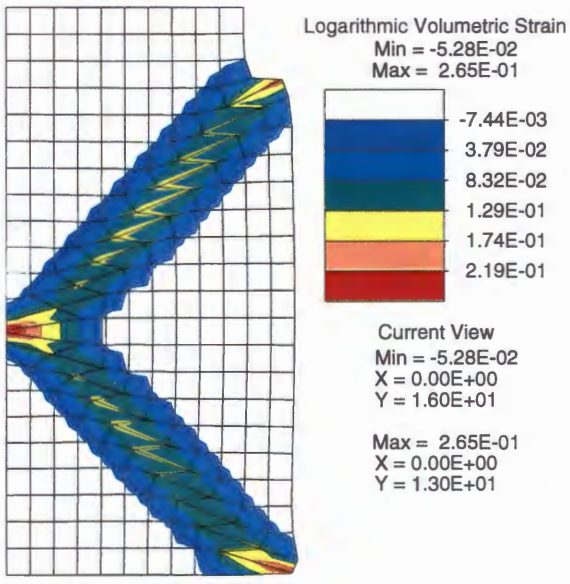

FIGURE 4.9. Plane strain compression test. Solutions at an imposed top vertical displacement of $\bar{v} = 5.0\ cm$ ($k_{h_o} = 5 \cdot 10^{-9}\ m/s$; no magnification of the deformations).

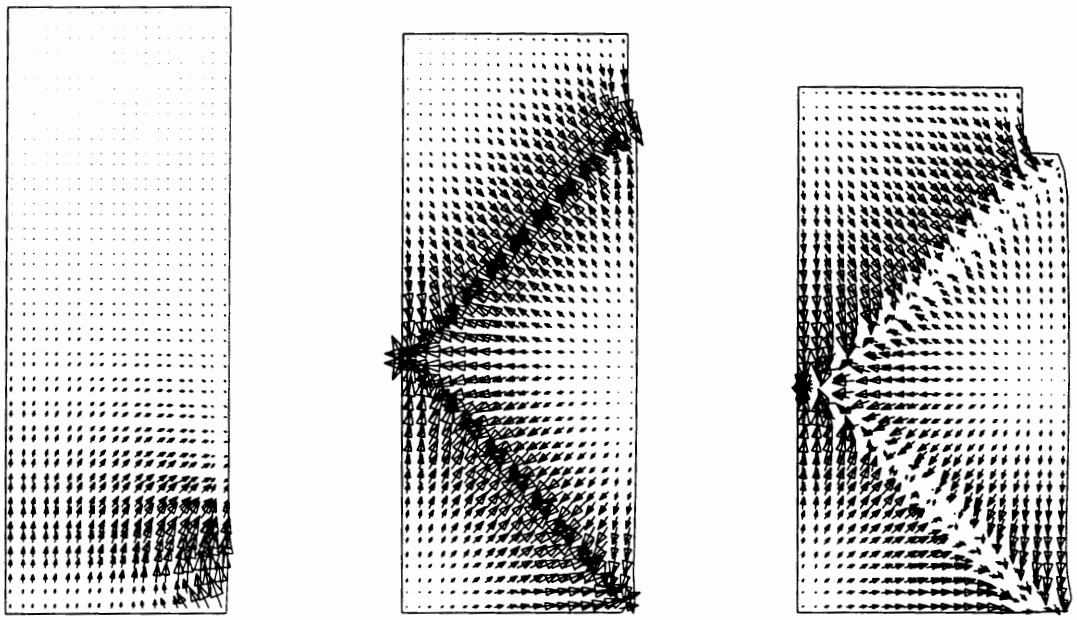

FIGURE 4.10. Plane strain compression test. Fluid flow vectors $\boldsymbol{q}_w$ at the quadrature points for two different imposed top vertical displacements: elastic solution $\bar{v} = 0.5\ cm$, and at two stages during localization, $\bar{v} = 2.0\ cm$ and $\bar{v} = 5.0\ cm$ ($k_{ho} = 5 \cdot 10^{-9}\ m/s$; no magnification of the deformations).

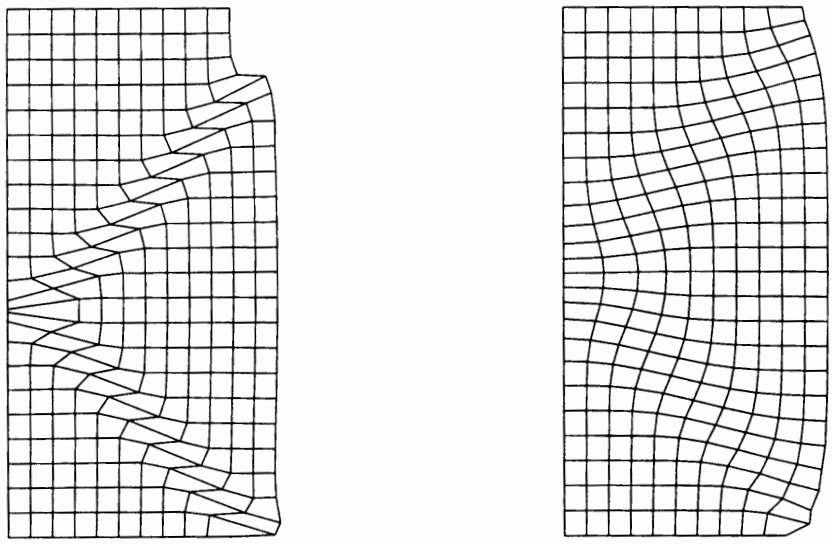

FIGURE 4.11. Plane strain compression test. Deformed configurations at $\bar{v} = 5.0\ cm$ obtained for two different hydraulic permeabilities, $k_{ho} = 5 \cdot 10^{-9}\ m/s$ and $k_{ho} = 5 \cdot 10^{-22}\ m/s$ (no magnification of the deformations). Observe that the low permeability precludes the development of strain localization when compared with the solution with higher permeability.

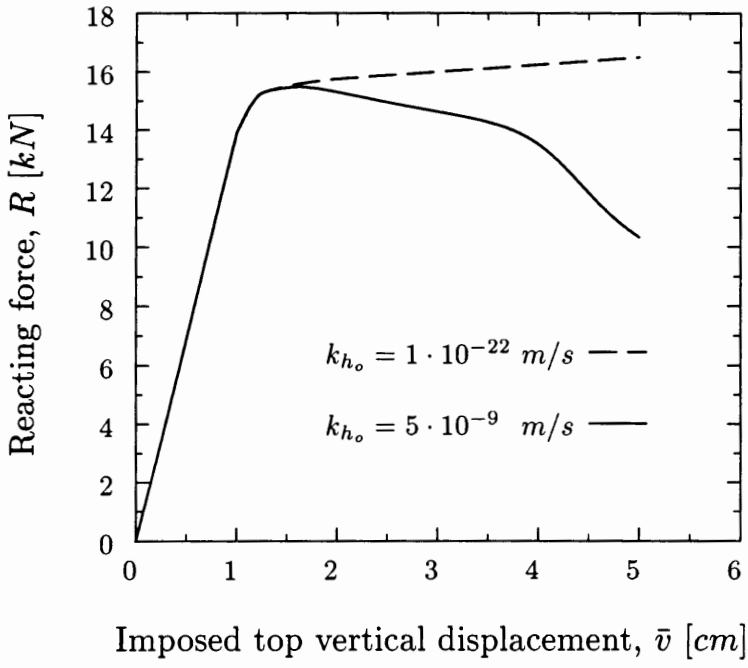

FIGURE 4.12. Plane strain compression test. Computed reaction force versus imposed top vertical displacement curves for two different permeabilities ($k_{h_o} = 5 \cdot 10^{-9}$ m/s and $k_{h_o} = 1 \cdot 10^{-22}$ m/s).

strain α, and logarithmic volumetric strain ε_v for two values of the imposed displacement $\bar{v} = 1$ cm and $\bar{v} = 5$ cm. These values correspond to the solutions before and after strain localization, which is clearly shown by the formation of two shear bands through the specimen. We note that the non-symmetry of the boundary conditions (in particular, the stick boundary conditions at the bottom) are enough to trigger the formation of the shear bands without the need of any imperfection. The shear bands are observed to form at the bottom right corner of the specimen and propagate in a straight manner through the specimen. We note again that symmetry conditions are imposed at the center of the specimen. Only the right half of the specimen is depicted in these figures.

We observe that the localized plastic response along the bands leads to a concentration of the fluid content in them. We first note the dilatant character of the assumed Drucker-Prager model. In particular, we refer to equation $(3.37)_3$ identifying the increase of the plastic part of the fluid content due to the plastic dilatancy. The total logarithmic volumetric strain has also been depicted in Figures 4.8 and 4.9, to observe the localization of this strain following the same trend as the the equivalent plastic strain. We have included in Figure 4.10 a plot of the fluid flow vectors $\boldsymbol{q}_w$ for different values of imposed vertical displacement, including an early purely elastic stage of the solid and two different

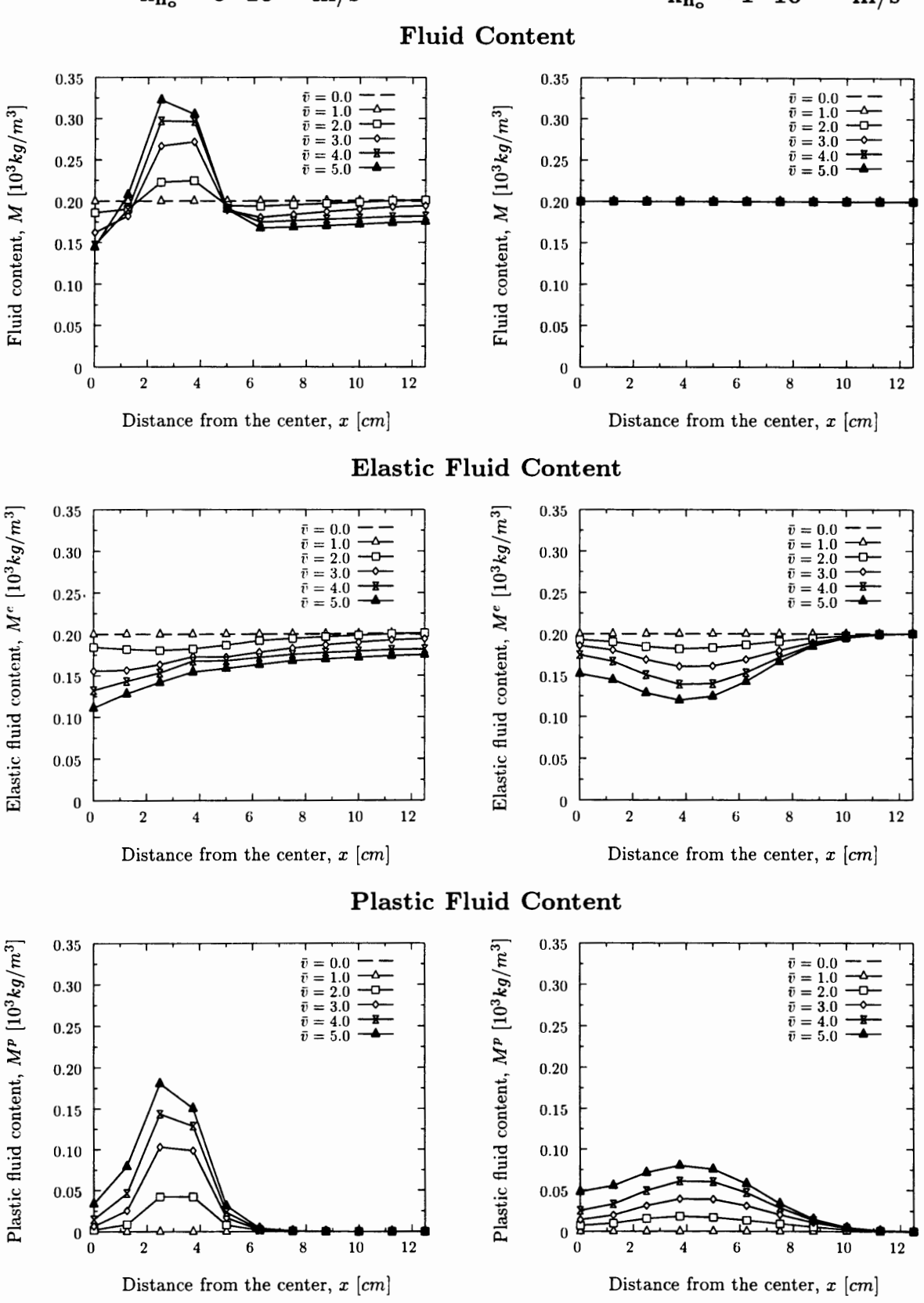

FIGURE 4.13. a. Plane strain compression test. Distribution at $y = H/3$ from the bottom of the fluid content M, and its elastic and plastic parts ($M = M^e + M^p$), for two different permeabilities ($k_{h_o} = 5 \cdot 10^{-9}\ m/s$ and $k_{h_o} = 1 \cdot 10^{-22}\ m/s$) and for different imposed top vertical displacements $\bar{v}$.

$\mathbf{k_{h_o} = 5 \cdot 10^{-9}\ m/s}$ $\mathbf{k_{h_o} = 1 \cdot 10^{-22}\ m/s}$

Logarithmic Volumetric Strain

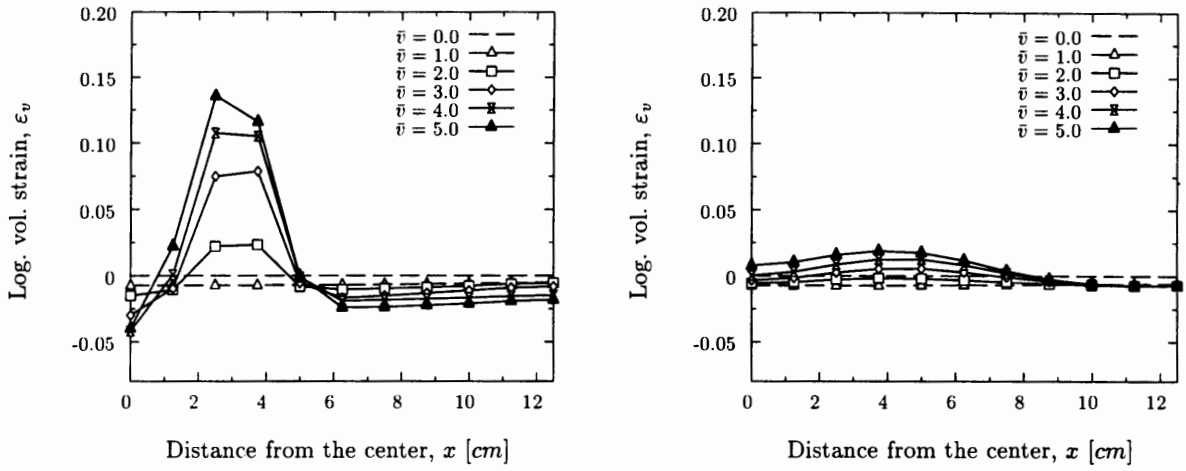

Elastic Logarithmic Volumetric Strain

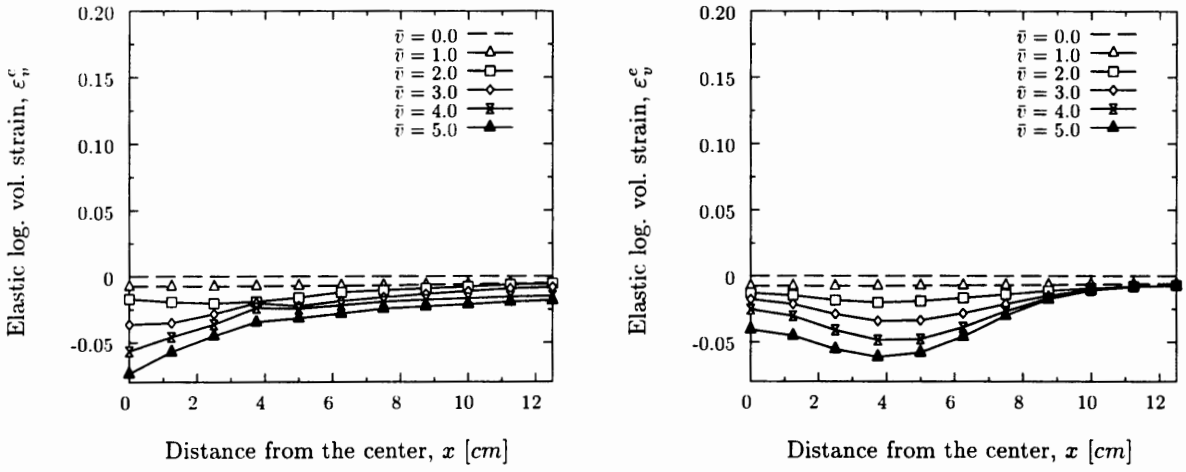

Plastic Logarithmic Volumetric Strain

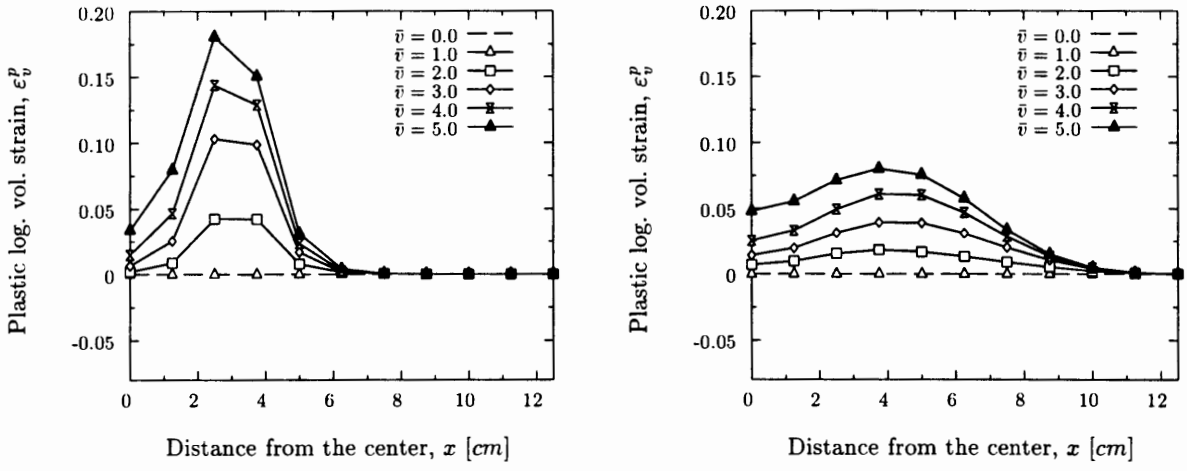

FIGURE 4.13.b. Plane strain compression test. Distribution at $y = H/3$ from the bottom of the logarithmic volumetric strain ε_v, and its elastic and plastic parts ($\varepsilon_v = \varepsilon_v^e + \varepsilon_v^p$), for two different permeabilities ($k_{h_o} = 5 \cdot 10^{-9}\ m/s$ and $k_{h_o} = 1 \cdot 10^{-22}\ m/s$). and for different imposed top vertical displacements $\bar{v}$.

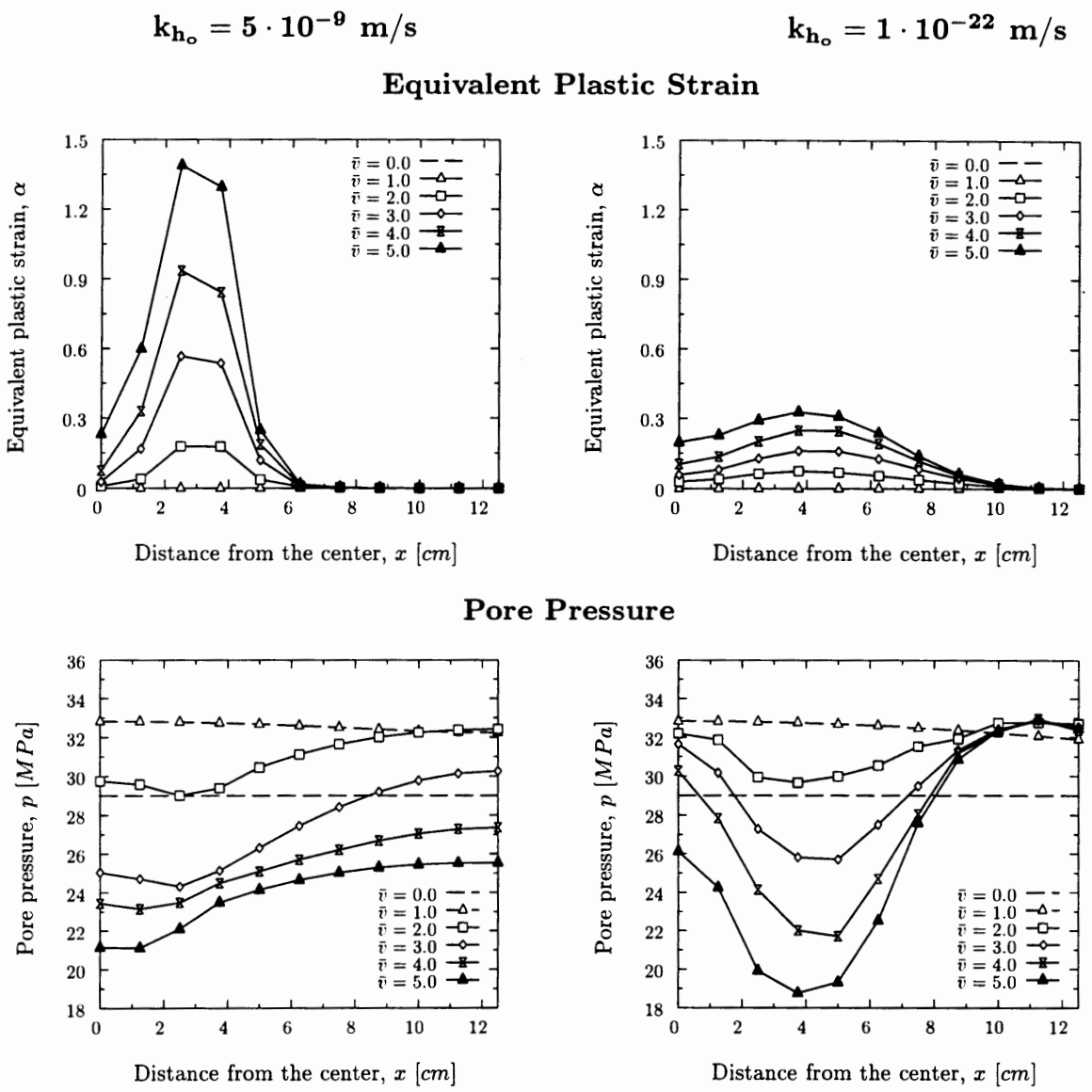

FIGURE 4.13c. Plane strain compression test. Distribution at $y = H/3$ from the bottom of the equivalent plastic strain α and the pore pressure p, for two different permeabilities ($k_{h_o} = 5 \cdot 10^{-9}$ m/s and $k_{h_o} = 1 \cdot 10^{-22}$ m/s). and for different imposed top vertical displacements $\bar{v}$.

stages in the localization process. The change in the pattern of the fluid flow once the shear band forms is clear from these plots. In particular, we observe that the shear band with its associated dilatancy and lower pore pressure drains the fluid flow from the rest of specimen.

The load-displacement curve obtained in this simulation is reported in Figure 4.12. The characteristic softening response common in localized solutions can be observed. We have also included the load-displacement curve obtained for the case of a very low permeability $k_{h_o} = 1 \cdot 10^{-22}$ m/s, recovering effectively the fully undrained case. We do not

observe in this situation this drop in the load applied to the specimen as the top deflection increases. Instead, a monotonically increasing curve is obtained. This situation is due to the load carrying capacity of the incompressible fluid, which is now unable to dissipate the excess pore pressure due to the very low permeability of the solid.

This extra load carrying capacity added by the fluid in the very low permeability solution leads also to a delay of the transfer of the load to the solid's skeleton. This leads to a completely different pattern of the deformation of the solid. We have included in Figure 4.11 the deformation obtained for both solutions at the imposed vertical displacement of $\bar{v} = 5\ m$. The clear presence of the shear band in the higher permeability solution is to be contrasted with a lack of strain localization in the low permeability solution. Smooth bulging is observed in the specimen instead.

To compare both solutions in more detail, we have included in Figures 4.13.a to 4.13.c the distribution of different quantities along an horizontal cut at a distance $H/3$ from the bottom of the specimen for different imposed vertical displacements $\bar{v}$. These figures show clearly the development of the shear band for the higher permeability solution $k_{h_o} = 5 \cdot 10^{-9}\ m/s$ (left column). Observe, in particular, the gradual localization of the equivalent plastic strain. As noted above, we can observe the concentration of the fluid content M in the band, with its main contribution being the plastic part M^p due to the associated localized plastic dilatancy ε_v^p. The volumetric strain outside the band is seen to be much smaller than in the band, consistent with the almost incompressible response of the porous solid in the elastic range due to the strong fluid coupling. Note also the associated drop in the pore pressure in all the specimen as the band develops from an increased value during the initial elastic stages of the deformation.

This situation is to be contrasted with the response in the undrained limit (right column). We can observe how basically all the quantities show a more uniform distribution when compared with the localized solution. Still, slight concentrations around what it is essentially the same position of the band for the high permeability solution can be observed, but with much smaller values of these concentrations. Note that the pore pressure eventually drops around that position, but the pore pressure level in the rest of the specimen remains high compared to the high permeability solution, and close to the values attained during the early stages of elastic deformation. We note the effectively absent fluid flow, as reflected by the constant distribution of the fluid content $M \approx M_o$. Still, the plastic response with the corresponding plastic dilatancy leads to a local transfer of fluid content from elastic M^e to plastic M^p. This delay in the formation and propagation of shear bands in highly undrained conditions is in agreement with the observed experimental results, analyses and numerical simulations reported in the literature. We refer to the numerical simulations presented in LORET & PREVOST [1991], and the analyses and reported experimental results in VARDOULAKIS [1996a,b], among others.

5. Concluding Remarks

The previous developments illustrate the use of the multiplicative elastoplastic decomposition of the deformation gradient in the modeling of poro-plastic porous solids in the finite strain range. This strategy allows for the developments of constitutive models in a fully consistent thermodynamic framework, extending in this way the original formulations of Biot to this finite strain poro-plastic case. This thermodynamic framework has shown to be crucial in the characterization of the dissipative structure of the final coupled initial-boundary value problem. To that purpose, we have presented the formulation of an a-priori stability estimate for the problem of evolution. Regarding the numerical schemes, we have presented complete details of the final expressions in the finite element implementation of the proposed models. In addition, the conformity of numerical schemes based on an undrained partition of the coupled problem with the aforementioned dissipative structure identifies the numerical stability inherent in these schemes.

The formulation of stable staggered methods for physically coupled problems has been one of the main driving goals in the previous research in the field. We believe that the dissipative framework identified in the paper and its approximation by different partitions of the problem lead to the identification of the origin of the instabilities observed in standard staggered solutions of this type of problems. The numerical results reported herein confirm the superior stability properties of the schemes based on the undrained split in contrast with the drained split. However, the first order of accuracy of all these staggered schemes may be an issue for long-term simulations in strongly coupled problems. Appreciable errors can accumulate for large values of the time step in strongly coupled problems, especially in the path dependent elastoplastic case. This situation applies especially to the stable schemes, given the ability to consider these large time steps. In particular, we have observed that in these circumstances stable schemes based on an undrained solid phase may lead to overly stiff response due to the quasi-incompressible character of this phase as the Biot's modulus Q increases; see the discussion of the results reported in Section 4.1 above. The study of second order alternatives through, for example, multiple pass techniques is then of the main interest, and constitutes our current focus in this area.

Acknowledgments: Financial support for this research has been provided by the ONR under contract no. N00014-96-1-0818 with UC Berkeley. We acknowledge also the support of the NSF under contract no. CMS-9703000 with UC Berkeley.

References

ARMERO, F. & CALLARI, C. [1998] "Strong Discontinuities in Fully Saturated Porous Media," submitted to *Proc. 4th World Congr. Comp. Mech,,* to be held in Buenos Aires, June 1998.

ARMERO, F. & SIMO, J.C. [1992] "A new unconditionally stable fractional step method for nonlinear coupled thermomechanical problems", *Int. J. Num. Meth. Engr.,* **35**, 737-766.

ARMERO, F. & SIMO, J.C. [1993] "A–priori stability estimates and unconditionally stable product formula algorithms for nonlinear coupled thermoplasticity", *Int. J. Plast.,* **9**, 749-782.

ARMERO, F. & SIMO, J.C. [1996], "Formulation of a New Class of Fractional-Step Methods for the Incompressible MHD Equations that Retains the Long-Term Dissipativity of the Continuum Dynamical System", *Integration Algorithms for Classical Mechanics,* The Fields Institute Communications, 10, 1-23.

BALL, J.M. & KNOWLES, G. [1986], "Lyapunov Functions for Thermomechanics with Spatially Varying Boundary Temperatures", *Arch. Rat. Mech. Analysis,* **92**, 193–204.

BEAR, J. [1972], *Dynamics of Fluids in Porous Media,* Dover Publ., New York.

BENALLAL, A. & COMI C. [1997], "Properties of Finite-Step Problem in Numerical Analysis of Unstable Saturated Porous Continua," *Proc. Comp. Plasticity V,* ed. D.R.J. Owen, E. Oñate, & E. Hinton, CIMNE, Barvelona, 1612-1616.

BIOT, M.A. [1941], "General Theory of Three–Dimensional Consolidation", *J. Appl. Phys.,* **12** 155-164.

BIOT, M.A. [1954], "Theory of Stress-Strain Relations in Anisotropic Viscoelasticity and Relaxation Phenomena," *J. App. Phys.,* **25** 1385–1391.

BIOT, M.A. [1955], "Theory of elasticity and consolidation for a porous anisotropic solid", *J. App. Phys.,* **26** 182–185.

BIOT, M.A. [1956a], "Thermoelasticity and Irreversible Thermodynamics," *J. App. Phys.,* **27** 240–253.

BIOT, M.A. [1956b], "Theory of Deformation of a Porous Viscoelastic Anisotropic Solid" *J. App. Phys.,* **27** 459-467.

BIOT, M.A. [1972], "Theory of Finite Deformations of Porous Solids," *Ind. Univ. Math. Journal,* **21** 597-620.

BOOKER, J.R. & SMALL, J.C. [1975], "An Investigation of the Stability of Numerical Solutions of Biot's Equations of Consolidation," *Int. J. Solids Structures,* **11**, 907-917.

BORJA, R.L. & ALARCON, E. [1995], "A Mathematical Framework for Finite Strain Elastoplastic Consolidation. Part I: Balance Laws, Variational Formulation, and Linearization," *Comp. Appl. Mech. Engr.*, **122**, 145-171.

CARTER, J.P.; BOOKER, J.R. & SMALL, J.C., [1979], "The Analysis of Finite Elasto-Plastic Consolidation," *Int. J. Num. An. Meth. Geomech.*, **3**, 107-129.

CHRISTIAN, J.T. [1977], "Two- and Three-Dimensional Consolidation," *Numerical Methods in Geothechnical Engineering,* ed. by C.S. Desai and J.T. Christian, MacGraw Hill, New York, 399-426.

COLEMAN, B.D. & DILL E.H. [1973] "On Thermodynamics and the Stability of Motions of Materials with Memory", *Arch. Rat. Mech. Analysis,* **51**, 1–53.

COUSSY, O. [1995] *Mechanics of Porous Media,* John Wiley & Sons, Chichester.

CUITINHO, A.M. & ORTIZ, M. [1992], "A Material-Independent Method for Extending Stress Update Algorithms from Small-Strain Plasticity to Finite Plasticity with Multiplicative Kinematics," *Eng. Comp.*, **9**, 437-451.

DAFERMOS, C.M. [1976], "Contraction Semigroups and Trend to Equilibrium in Continuum Mechanics", *Springer Lecture Notes in Math.*, **503**, 295–306.

DUHEM, P. [1911], *Traité d'Energetique ou de Thermodynamique Générale,* Gauthier Villars, Paris.

ERICKSEN, J.L. [1966], "Thermoelastic Stability", *Proc.* 5^{th} *National Cong. Appl. Mech.*, 187–193.

ETEROVICH, A.L. & BATHE, K.J. [1990], "A Hyperelastic Based Large Strain Elasto-Plastic Constitutive Formulation with Combined Isotropic-Kinematic Hardening Using Logarithmic Stresses and Strain Measures," *Int. J. Num. Meth. Engr.*, **30**, 1099-1115

GLASER & ARMERO [1997] "On the Formulation of Enhanced Strain Finite Elements in Finite Deformations," *Eng. Comp.*, **14**, 759-791.

GOVINDJEE, S. & SIMO, J.C. [1991] "Coupled Stress Diffusion: Case II," *J. Mech. Phys. Solids,* **41**, 863-887.

GURTIN, M.E. [1975], "Thermodynamics and Stability", *Arch. Rat. Mech. Analysis,* **59**, 53–96.

KOITER, W.T. [1953], "Stress-Strain Relations, Uniqueness and Variational Theorems for Elastic-Plastic Materials with Singular Yield Surface," *Quarter. Appl. Math.*, **11**, 350-354.

LORET, B. & PREVOST, J.H. [1993] "Dynamic Strain Localization in Fluid-Saturated Porous Media," *J. Eng. Mechanics,* **117**, 907-922.

LEE, E.H. AND LIU, D.T. [1967], "Finite Strain Elastic-Plastic Theory Particularly for Plane Wave Analysis," *J. Appl. Phys.*, **38**.

LEE, E.H. [1969], "Elastic-plastic Deformation at Finite Strains", *J. Appl. Mech.*, **36**, 1–6.

LEWIS, R.W. & SCHREFLER, B.A. [1987], *The Finite Element Method in the Deformation and Consolidation of Porus Media,* Wiley.

LUBLINER, J. [1986], "Normality Rules in Large-deformation Plasticity", *Mech. Mat.*, **5**, 29–34.

MANDEL, J. [1971], *Plasticité Classique et Viscoplasticité,* International Centre of Mechanical Sciences, Course 97, Udine, Springer Verlag.

MARSDEN, J. & HUGHES, T.J.R. [1983] *Mathematical Foundations of Elasticity,* Dover Pub., New York.

MOREAU, J.J. [1976], "Applications of Convex Analysis to the Treatment of Elastoplastic Systems," in *Applications of Methods of Functional Analysis to Problems in Mechanics,* ed. P. Germain and B. Nayroles, Springer-Verlag, Berlin.

PARK, K.C. [1983], "Stabilization of partitioned solution procedure for fluid–soil interaction analysis", *Int. J. Num. Meth. Engr.*, **19**, 1669-1673.

PARK, K.C. & FELIPPA, C.A [1983], "Partitioned Analysis of Coupled Problems", in *Computational Methods in Transient Analysis,* (ed. by T. Belytschko and T.J.R. Hughes), North Holland.

PREVOST, J.H. [1981] "Consolidation of Anelastic Porous Media," *J. Eng. Mech. Div. ASCE,* **107** (EM1), 169-186.

PREVOST, J. [1983] "Implicit-Explicit Schemes for Nonlinear Consolidation," *Comp. Meth. Appl. Mech. Engr.*, **39**, 225-239.

SANDHU, R.S. & WILSON, E.L. [1969] "Finite Element Analysis of Seepage in Elastic Media," *J. Engr. mech. Div. ASCE,* **95** (EM3, 641-652.

SCHREFLER, B.A.; MAJORANA, C.E. & SANAVIA, L. [1995] "Shear Band Localization in Saturated Porous Media" *Arch. Mech.* **47**, 577-599.

SCHREFLER, B.A.; SANAVIA, L. & GAWIN, D. [1997] "Strain Localisation Modelling in Fully and Partially Saturated Porous Media, *Proc. Comp. Plasticity V,* ed. D.R.J. Owen, E. Oñate, & E. Hinton, CIMNE, Barvelona.

SIMO, J.C. [1992], "Algorithms for static and dynamic multiplicative plasticity that preserve the classical return mapping schemes of the infinitesimal theory", *Comp. Meth. Appl. Mech. Engr.*, **98**, 41-104.

SIMO, J.C. [1994] "Numerical Analysis of Classical Plasticity", *Handbook for Numerical Analysis, Volume IV,* ed. by P.G. Ciarlet and J.J. Lions, in press.

SIMO, J.C. & MIEHE C. [1992] "Associative coupled thermoplasticity at finite strains: formulation, numerical analysis and implementation", *Comp. Meth. App. Mech. Engnr.,* **98**, 41-104.

SIMO, J.C. & ORTIZ, M. [1985] "A Unified Approach to Finite Deformation Elastoplastic Analysis Based on the Use of Hyperelastic Constitutive Equations," *Comp. Meth. Appl. Mech. Engr.,* **49**, 221-245.

SMALL, J.C.; BOOKER, J.R. & DAVIS, E.H. [1976], "Elasto-Plastic Consolidation of Soil," *Int. J. Solids Structures,* **12**, 431-448.

TRUESDELL & NOLL [1965] "The Nonlinear Field Theories of Mechanics," *Handbich der Physik Bd. III/3,* ed. by S. Fluegge, Springer Verlag, Berlin.

TURSKA, E. & SCHREFLER, B.A. [1993], "On Convergnece Conditions of Partitioned Solution Procedures for Consolidation Problems," *Comp. Meth. App. Mech. Engnr.,* **106**, 51-63.

VARDOULAKIS, I. [1996a] "Deformation of Water-Saturated Sand: I. Uniform Undrained Deformation and Shear Banding. Shear Banding," *Géotechnique,* **46**, 441-456.

VARDOULAKIS, I. [1996b] "Deformation of Water-Saturated Sand: II. Effect of Pore Water Flow and Shear Banding," *Géotechnique,* **46**, 457-472.

WEBER, G. & ANAND, L. [1990], "Finite Deformation Constitutive Equations and Time Integration Procedure for Isotropic, Hyperelastic-Viscoplastic Solids," *Comp. Meth,. Appl. Mech. Engr.,* **79**, 173-202.

WOOD, W.L. [1990], *Practical Time Stepping Schemes,* Clarendon, Oxford University Press.

YANENKO, N.N. [1971], *The Method of Fractional Steps,* Springer Verlag, New York.

ZIENKIEWICZ, O.C.; CHANG, C.T. & BETTES, P. [1980], "Drained, Undrained, Consolidating and Dynamic Behaviour Assumptions in Soilds," *Géotechnique,* **30**, 385-395.

ZIENKIEWICZ, O.C. & HUMPHESON, C. [1977], "Viscoplasticity: a Generalized Model for Description of Soil Behavior," *Numerical Methods in Geothechnical Engineering,* ed. by C.S. Desai and J.T. Christian, MacGraw Hill, New York, 116-147.

ZIENKIEWICZ, O.C.; PAUL, D.K. & CHAN, A.H. [1988], "Unconditionally Stable Staggered Solution Procedure for Soil–pore Fluid Interaction Problems", *Int. J. Num. Meth. Engr.,* **26**, 1039–1055.

ZIENKIEWICZ, O.C. & TAYLOR, R.L. [1991] *The Finite Element Method, Volume 2,* McGraw Hill, London.

Appendix I. Finite Element Implementation

We summarize in this appendix the numerical implementation of the finite strain poro-plastic model described in the paper. To this purpose, we first summarize the weak form of the governing equations of the problem.

i. *The weak equations.* Standard arguments lead to the weak form of the equilibrium equation (2.10)

$$\int_{\mathcal{B}} \boldsymbol{\tau} : \mathrm{sym}\,[\nabla(\delta\boldsymbol{\varphi})]\; dV = \int_{\mathcal{B}} \rho_o \boldsymbol{f} \cdot \delta\boldsymbol{\varphi}\; dV + \int_{\partial_T \mathcal{B}} \bar{\boldsymbol{T}} \cdot \delta\boldsymbol{\varphi}\; dA\,, \tag{I.1}$$

for all admissible variations (that is, satisfying the homogeneous essential boundary conditions $(2.24)_1$). Similarly, the weak form of the conservation of fluid mass equation is written as

$$\int_{\mathcal{B}} \dot{M}\; \delta p\; dV - \int_{\mathcal{B}} \hat{\boldsymbol{q}}_w \cdot \nabla(\delta p)\; dV = \int_{\partial_Q \mathcal{B}} \bar{Q}_w\; \delta p\; dA\,, \tag{I.2}$$

for all admissible variations of the pore pressure field (that is, satisfying homogeneous essential boundary conditions $(2.26)_1$). Here, we have introduced the notation $\hat{\boldsymbol{q}}_w := J\boldsymbol{q}_w = \boldsymbol{F}\boldsymbol{Q}_w$, as defined by the Piola transform (2.6).

ii. *The finite element residuals.* We consider a finite element discretization $\mathcal{B} = \cup_{e=1}^{n_{\mathrm{elem}}} \Omega_e^h$ of the domain of interest $\mathcal{B}$ as a basis for the interpolation of the displacement and pore pressure fields

$$\boldsymbol{u}\Big|_{\Omega_e^h} = \boldsymbol{\varphi}(\boldsymbol{X}) - \boldsymbol{X} = \boldsymbol{N}_u^T \boldsymbol{d} \qquad \text{and} \qquad p\Big|_{\Omega_e^h} = \boldsymbol{N}_p^T \boldsymbol{p}\,, \tag{I.3}$$

with nodal displacements $\boldsymbol{d}$ and nodal pore pressures $\boldsymbol{p}$, and corresponding set of element shape functions $\boldsymbol{N}_u = [N_u^A]$ and $\boldsymbol{N}_p = [N_p^A]$ ($A = 1, n_{\mathrm{node}u,p}$ = number of displacement/pore pressure nodes in element Ω_e^h). Standard arguments lead to the discrete finite element equations

$$\left.\begin{aligned} \boldsymbol{R}_{\boldsymbol{u}_{n+1}} &:= \boldsymbol{f}^{ext}_{u_{n+1}} - \mathop{\mathbf{A}}_{e=1}^{n_{\mathrm{elem}}} \int_{\Omega_e^h} \boldsymbol{b}^T_{u_{n+1}} \boldsymbol{\tau}_{n+1}\; dV = 0\,, \\ \boldsymbol{R}_{p_{n+1}} &:= \boldsymbol{f}^{ext}_{p_{n+1}} - \mathop{\mathbf{A}}_{e=1}^{n_{\mathrm{elem}}} \int_{\Omega_e^h} \left[\boldsymbol{N}_p^T \frac{1}{\Delta t} \left(M_{n+1} - \tilde{M}_{n+1} \right) - \boldsymbol{b}^T_{p_{n+1}} \hat{\boldsymbol{q}}_{w_{n+1}} \right] dV = 0\,, \end{aligned}\right\} \tag{I.4}$$

where the symbol $\mathbf{A}_{e=1}^{n_{\mathrm{elem}}}$ denotes the assembly over the different n_{elem} elements. A typical time step $[t_n, t_{n+1}]$, with $\Delta t = t_{n+1} - t_n$, has been considered in (I.4). The converged values of the nodal displacements $\boldsymbol{d}_n$, nodal pore pressures $\boldsymbol{p}_n$ and internal variables $\{\boldsymbol{b}_n^e, \alpha_n, M_n^p\}$ at the end of the previous time step are assumed known.

The linearized strain operator $\boldsymbol{b}_u$ is defined as

$$\boldsymbol{b}_u = [\, \boldsymbol{b}_u^1 \quad \dots \quad \boldsymbol{b}_u^{n_{\text{node}u}} \,] \;, \quad \text{where} \quad \boldsymbol{b}_u^A = \begin{bmatrix} N^A_{u,1} & 0 \\ 0 & N^A_{u,2} \\ N^A_{u,2} & N^A_{u,1} \end{bmatrix} \quad \text{for } A = 1, n_{\text{node}u} \;, \tag{I.5}$$

for, e.g., the two dimensional case $n_{\text{dim}} = 2$. Similarly, the discrete gradient operator

$$\boldsymbol{b}_p = [\, \boldsymbol{b}_p^1 \quad \dots \quad \boldsymbol{b}_p^{n_{\text{node}p}} \,] \;, \quad \text{where} \quad \boldsymbol{b}_u^A = \begin{bmatrix} N^A_{p,1} \\ N^A_{p,2} \end{bmatrix} \quad \text{for } A = 1, n_{\text{node}p} \;, \tag{I.6}$$

is considered in $(\text{I}.4)_2$. The different components $(\cdot)_{,i}$ of the spatial gradient of the shape functions in a Cartesian reference system have been considered in these expressions.

In $(\text{I}.4)_1$, we consider the stresses $\boldsymbol{\tau}_{n+1} = \boldsymbol{\tau}(\boldsymbol{d}_{n+1}, \tilde{\boldsymbol{p}})$, evaluated at $\boldsymbol{d}_{n+1}$ and $\tilde{\boldsymbol{p}}$, where $\tilde{\boldsymbol{p}} = \boldsymbol{p}_{n+1}$ for the monolithic scheme, and $\tilde{\boldsymbol{p}} = \boldsymbol{p}_n$ for the drained split. Iterative Gauss-Seidel schemes are obtained through a multiple-pass strategy, with $\tilde{\boldsymbol{p}} = \boldsymbol{p}_{n+1}^{(k)}$ the value of the pore pressure in the last iteration. For the undrained split, the nodal pressures are not changed when solving $(\text{I}.4)_1$ during the solid phase. Instead, the constant fluid content equation is imposed locally at the quadrature points

$$M_n^e + M_n^p = \widehat{M}^e(\boldsymbol{d}_{n+1}, \tilde{p}) + \widehat{M}^p(\boldsymbol{d}_{n+1}, \tilde{p}) \;, \tag{I.7}$$

leading to the local pore pressure $\tilde{p}$. See Box 3.2 for details. For the simple case given by (3.36) and an incompressible fluid (3.26), the linear expression

$$\tilde{p}_{n+1} = p_n - Q\, b \left(\varepsilon_{v_{n+1}} - \varepsilon_{v_n}\right) \;, \tag{I.8}$$

is obtained. The quasi-incompressible character of the undrained solid phase for large values of $\delta = b^2 Q / \kappa_{sk}$ is apparent. We refer to ARMERO & SIMO [1992,93] for complete analyses of the numerical properties of these different methods.

The numerical schemes based on the drained and undrained splits proceed then by solving equations (I.4) in a staggered manner, with a first solid phase corresponding to the solution of $(\text{I}.4)_1$ followed by a fluid phase corresponding to the solution of $(\text{I}.4)_2$ at a fixed configuration. Each phase involves a Newton-Raphson type scheme involving the linearization described below. Note that for the fluid phase of the undrained split we have

$$\dot{M} \approx \frac{1}{\Delta t}\left(M_{n+1} - \tilde{M}_{n+1}\right) = \frac{1}{\Delta t}\left(M_{n+1} - M_n\right) \;, \tag{I.9}$$

locally at each quadrature point, where the fluid content after the solid phase $\tilde{M}_{n+1}$ is known since $\tilde{M}_{n+1} = M_n$. Therefore, the final numerical implementation is independent of the value of the pore pressure $\tilde{p}$ after solving the undrained solid phase. The drained split uses also the approximation (I.9). Similarly, the fluid flow vector $\hat{\boldsymbol{q}}_{w_{n+1}}$ and the fluid

content M_{n+1} in the fluid equation $(I.4)_2$ are given by the constitutive relations developed in Sections 2.2 and 3.4, respectively.

iii. *Return mapping algorithm.* The numerical integration of the multiplicative poro-plastic model summarized in Box 3.1, for the stresses $\boldsymbol{\tau}_{n+1}$ and the update of the internal variables $\{\boldsymbol{b}^e_n, \alpha_n, M^p_n\} \to \{\boldsymbol{b}^e_{n+1}, \alpha_{n+1}, M^p_{n+1}\}$, is obtained through an exponential return mapping algorithm following similar arguments as in SIMO [1992], with additional considerations regarding the volumetric plastic response. For completeness, we outline here the main steps, and refer to this reference for additional details for the common considerations. The final equations are summarized in Box I.1. The reader is referred also to WEBER & ANAND [1990], ETEROVICH & BATHE [1990], and CUITINHO & ORTIZ [1992].

The development of the return mapping scheme starts with the consideration of the classical elastic predictor/plastic corrector split, which for the flow rule (??) is based on the partition

$$\boldsymbol{\pounds}_{\boldsymbol{v}}\boldsymbol{b}^e = \dot{\boldsymbol{b}}^e \underbrace{-\boldsymbol{l}\boldsymbol{b}^e - \boldsymbol{b}^e\boldsymbol{l}^T}_{\textit{elastic predictor}} = \underbrace{-2\gamma\, \boldsymbol{n}_{\Phi}\, \boldsymbol{b}^e}_{\textit{plastic corrector}} , \tag{I.10}$$

with the elastic predictor defining exactly the trial elastic state $\boldsymbol{b}^{e\,tr}_{n+1}$ as defined in Box I.1. Upon detecting an inadmissible trial state through $\Phi^{tr}_{n+1} \geq 0$, the plastic corrector uses the exponential mapping

$$\boldsymbol{b}^e_{n+1} = \exp\left[-2\Delta\gamma\ \boldsymbol{n}_{\Phi}\right] \boldsymbol{b}^{e\,tr}_{n+1} , \tag{I.11}$$

which leads to the relation

$$J^e_{n+1} = \exp\left[-2\Delta\gamma\ \mathrm{tr}(\boldsymbol{n}_{\Phi})\right] J^{e\,tr}_{n+1} , \tag{I.12}$$

for the elastic Jacobian. Noting that $\mathrm{tr}(\boldsymbol{n}_{\Phi}) = g'/\sqrt{2}$, the use of the assumed Hencky's law for the elastic response

$$\bar{\tau}'_{n+1} = \kappa_{sk} \log J^e_{n+1} \qquad \text{and} \qquad \mathrm{dev}[\boldsymbol{\tau}'_{n+1}] = \mu_{sk} \log \bar{\boldsymbol{b}}^e_{n+1} , \tag{I.13}$$

with $\bar{\boldsymbol{b}}^e_{n+1} := J^{e(-2/3)}\boldsymbol{b}^e_{n+1}$, leads to the relation

$$\bar{\tau}'_{n+1} = \bar{\tau}'^{\,tr}_{n+1} - \frac{\Delta\gamma}{\sqrt{2}}\, \kappa_{sk} g'(\bar{\tau}'_{n+1}) , \tag{I.14}$$

for the volumetric part, and

$$\mathrm{dev}[\boldsymbol{\tau}'_{n+1}] = \mathrm{dev}[\boldsymbol{\tau}'^{\,tr}_{n+1}] - 2\mu_{sk}\Delta\gamma \frac{\mathrm{dev}[\boldsymbol{\tau}'_{n+1}]}{\|\,\mathrm{dev}[\boldsymbol{\tau}'_{n+1}]\|} \implies \|\,\mathrm{dev}[\boldsymbol{\tau}'_{n+1}]\| = \|\,\mathrm{dev}[\boldsymbol{\tau}'^{\,tr}_{n+1}]\| - 2\mu_{sk}\Delta\gamma , \tag{I.15}$$

for the deviatoric part. The imposition of the consistency condition (3.14) at t_{n+1}, in combination with (I.13), to the expression

$$\frac{1}{\sqrt{2}}\Big(\|\,\mathrm{dev}\,\boldsymbol{\tau}'^{\,tr}_{n+1}\| + g(\bar{\tau}_{n+1})\Big) - [\tau_{yo} - q(\alpha_{n+1})] - 2\mu_{sk}\Delta\gamma = 0 . \tag{I.16}$$

The more general case of a linear viscoplastic model, in the Perzyna form (3.21), is easily incorporated by equating this last expression to $\Delta\gamma\eta_\phi/\Delta t$ instead. The system of two nonlinear equations (I.14) and (I.16) is solved for $\Delta\gamma \geq 0$ using a Newton scheme as described in Box I.1. For the case of linear hardening and linear volumetric response ($g(\bar{\tau}') = \beta_\phi\ \bar{\tau}'$), the following closed-form expression

$$\Delta\gamma = \frac{1}{\sqrt{2}\ \left(\mu_{sk} + \frac{1}{2}\kappa_{sk}\ \beta_\phi^2 + H\right)} \left[\| \operatorname{dev}[\boldsymbol{\tau}'^{tr}_{n+1}\| + \beta_\phi \bar{\tau}'^{tr}_{n+1} - \sqrt{2}(\tau_{yo} + H\alpha_n)\right] \geq 0\ , \quad \text{(I.17)}$$

is obtained. The plastic updates follow in principal directions making use of the isotropy of the model as summarized in Box I.1.

We note that the above considerations apply to the case of a smooth yield surface. In particular, the above solution is valid when it leads to $g(\bar{\tau}'_{n+1}) \leq g(\bar{\tau}'_{vertex\,n+1}) = \sqrt{2}\,(\tau_{yo} - q(\alpha_{n+1}))$ or, equivalently, $\| \operatorname{dev}[\boldsymbol{\tau}'_{n+1}\| \geq 0$ in $(\text{I.15})_2$ after solving (I.16). Otherwise, and as discussed in Remark 3.3, the flow rule (3.39) in the vertex of the Drucker-Prager model is activated, which involves the additional plastic multiplier $\Delta\gamma^{(2)}$ as

$$\bar{\tau}'_{n+1} = \bar{\tau}'^{tr}_{n+1} - \frac{\left(\Delta\gamma^{(1)} + \Delta\gamma^{(2)}\right)}{\sqrt{2}}\ \kappa_{sk} g'(\bar{\tau}'_{n+1})\ , \quad \text{(I.18)}$$

for the volumetric part, keeping (I.15) with $\Delta\gamma^{(1)}$ instead of $\Delta\gamma$. This case leads to the closest-point-projection to the vertex, with

$$\| \operatorname{dev}[\boldsymbol{\tau}'_{n+1}\| = 0 \qquad \Longrightarrow \qquad \Delta\gamma^{(1)} = \frac{1}{\sqrt{2}\mu_{sk}} \| \operatorname{dev}[\boldsymbol{\tau}'^{tr}_{n+1}\|\ , \quad \text{(I.19)}$$

and the consistency condition (I.16) simplified accordingly. A Newton shceme is again employed to determine $\Delta\gamma^{(2)}$, with the closed-form expression

$$\Delta\gamma^{(2)} = \frac{1}{H + \frac{1}{2}\kappa_{sc}\beta_\phi^2} \left[\frac{1}{\sqrt{2}}\beta_\phi \bar{\tau}'^{tr}_{n+1} - (\tau_{yo} + H\alpha_n)\right] - \frac{1}{\sqrt{2}\ \mu_{sc}} \| \operatorname{dev}[\boldsymbol{\tau}'^{tr}_{n+1}\|\ , \quad \text{(I.20)}$$

for the case of linear hardening and linear volumetric dependence. In this case, a simple calculation shows that $\Delta\gamma^{(2)} \geq 0$ when $\Delta\gamma$ given by (I.17) leads to an inadmissible solution ($\| \operatorname{dev}[\boldsymbol{\tau}'_{n+1}\| < 0$ in $(\text{I.15})_2$), so $\Delta\gamma^{(1)}$ in (I.19) is employed.

iv. *The linearized finite element equations.* The set of nonlinear equations (I.4) are solved using a Newton-Raphson scheme. The monolithic scheme leads to a non-symmetric fully coupled system in the nodal increments $\Delta\boldsymbol{d}$ and $\Delta\boldsymbol{p}$. For the staggered schemes under consideration, we have the consecutive solution of each phase with the respective linearized equations

$$\begin{aligned} \boldsymbol{K}^{(i)}_{uu_{n+1}} \Delta\boldsymbol{d}^{(i+1)}_{n+1} &= \boldsymbol{R}^{(i)}_{u_{n+1}}\ , \qquad \text{(solid phase)} \\ \boldsymbol{K}^{(i)}_{pp_{n+1}} \Delta\boldsymbol{p}^{(i+1)}_{n+1} &= \boldsymbol{R}^{(i)}_{p_{n+1}}\ , \qquad \text{(fluid phase)} \end{aligned} \quad \text{(I.21)}$$

for the increments of the nodal displacements $\Delta \boldsymbol{d} = \boldsymbol{d}^{(i+1)} - \boldsymbol{d}^{(i)}$ and nodal pore pressures $\Delta \boldsymbol{p}_{n+1}^{(i+1)} = \boldsymbol{p}_{n+1}^{(i+1)} - \boldsymbol{p}_{n+1}^{(i)}$, at iteration (i). To simplify the notation, the super-index (i) is omitted in the following developments.

As usual, the stiffness matrix consists of a material and geometric part,

$$\boldsymbol{K}_{uu_{n+1}} = \boldsymbol{K}_{m,uu_{n+1}} + \boldsymbol{K}_{g,uu_{n+1}} \ . \tag{I.22}$$

The expressions for the element contributions to the material part can be written as

$$\boldsymbol{K}^{AB}_{m,uu_{n+1}} = \int_{\Omega_e^h} \boldsymbol{b}^{A}_{u_{n+1}}{}^{T} \ \mathbf{c}_{n+1} \ \boldsymbol{b}^{B}_{u_{n+1}} \ dV \in \mathbb{R}^{n_{\text{dim}} \times n_{\text{dim}}} \ , \qquad (A, B = 1, n_{\text{node}_u}) \ , \tag{I.23}$$

where $n_{\text{dim}} = 2$ or 3 is the dimension of the space. The consistent algorithmic spatial tangent $\mathbf{c}_{n+1}$ defined by

$$\boldsymbol{\pounds}_{\Delta \boldsymbol{u}_{n+1}} \boldsymbol{\tau}_{n+1} = \mathbf{c}_{n+1} \ \text{sym}[\nabla(\Delta \boldsymbol{u}_{n+1})] \ , \tag{I.24}$$

has been used in (I.22). We have included in Box I.2 the closed-form expression of this tangent for the poro-plastic model summarized in Box 3.1. We note the symmetry of the final tangent for the considered associated poro-plastic model. The geometric stiffness contributions have the usual expression

$$\boldsymbol{K}^{AB}_{g,uu_{n+1}} = \left[\int_{\Omega_e^h} \nabla_{n+1} N_u^A \cdot \boldsymbol{\tau}_{n+1} \nabla_{n+1} N_u^B \ dV \right] \mathbf{1} \qquad (A, B = 1, n_{\text{node}}) \ , \tag{I.25}$$

where $\mathbf{1}$ is the $n_{\text{dim}} \times n_{\text{dim}}$ identity matrix.

The *fluid phase* involves the constant configuration defined by $\boldsymbol{d}_{n+1}$, avoiding then any additional geometric contributions in the linearized equations. Furthermore, for an effective stress model as considered in Section 3.4, we have no evolution of the inelastic internal variables $\{\boldsymbol{b}^e_{n+1}, \alpha_{n+1}, M^p_{n+1}\}$. This is the case since a change of pore pressure does not lead to a change of effective stresses if the configuration of the solid remains fixed. The tangent stiffness is then given by

$$\begin{aligned} \boldsymbol{K}^{AB}_{pp_{n+1}} = & \int_{\Omega_e^h} \rho_{w_o} \ \boldsymbol{b}^{A^T}_{p_{n+1}} \ \boldsymbol{k}_{o_{n+1}} \ \boldsymbol{b}^{B}_{p_{n+1}} \ dV \\ & + \int_{\Omega_e^h} \frac{c_{n+1}}{\Delta t} \ N_p^A \ N_p^B \ dV \in \mathbb{R} \qquad (A, B = 1, n_{\text{node}_p}) \ , \end{aligned} \tag{I.26}$$

for the permeability tensor $\boldsymbol{k}_{o_{n+1}}$ and hydraulic capacity $c_{n+1} = \partial M_{n+1} / \partial p_{n+1}$. For the model developed in Section 3.4, we have $c_{n+1} = \rho_{w_o} / Q$.

Remarks I.1. The simulations presented in Section 4 consider the Q1/ET4 enhanced strain finite element proposed in GLASER & ARMERO [1997]. We note the quasi-incompressible character of the undrained solid phase due to the fluid coupling and, consequently, the need of locking-free finite elements. One of the main features of these elements is their fully strain-driven structure. In this way, the above developments extend to this case by basically modifying the gradients used in the linearized strain operators through a set of enhanced strain parameters. These parameters are defined at the element level, allowing for their static condensation at this level. We refer to the aforementioned reference for complete details in the implementation. We note again that the return mapping algorithm and algorithmic consistent tangent summarized in Boxes I.1 and I.2, respectively, do not need any modification, and are used directly in the implementation of these enhanced elements. □

BOX I.1.a. Return mapping algorithm for the generalized Drucker-Prager poro-plastic model summarized in Box 3.1.

1. *Kinematics:*

1.1. Given the current displacement iterate $\boldsymbol{u}_{n+1}(\boldsymbol{X}) = \boldsymbol{\varphi}_{n+1}(\boldsymbol{X}) - \boldsymbol{X}$, compute the relative deformation gradient $\boldsymbol{f}_{n+1}$

$$\boldsymbol{f}_{n+1} := \boldsymbol{F}_{n+1}\boldsymbol{F}_n^{-1} = \left[\mathbf{1} - \nabla_{\boldsymbol{x}_{n+1}}\boldsymbol{u}_{n+1}\right]^{-1} ,$$

where $\boldsymbol{x}_{n+1} := \boldsymbol{\varphi}_{n+1}(\boldsymbol{X}) = \boldsymbol{X} + \boldsymbol{u}_{n+1}(\boldsymbol{X})$.

1.2. Compute the trial elastic left Cauchy-Green tensor from previously converged $\boldsymbol{b}^e_n$

$$\boldsymbol{b}^{e\,tr}_{n+1} := \boldsymbol{f}_{n+1}\boldsymbol{b}^e_n\boldsymbol{f}^T_{n+1} .$$

1.3. Compute the spectral decomposition

$$\boldsymbol{b}^{e\,tr}_{n+1} = \sum_{A=1}^{3} \left(\lambda^{e\,tr}_{A\,n+1}\right)^2 \boldsymbol{n}^{tr\,(A)}_{n+1} \otimes \boldsymbol{n}^{tr\,(A)}_{n+1} ,$$

The trial elastic Jacobian is then given by

$$J^{e\,tr}_{n+1} = \lambda^{e\,tr}_{1\,n+1}\,\lambda^{e\,tr}_{2\,n+1}\,\lambda^{e\,tr}_{3\,n+1} \qquad \text{and} \qquad \bar{\lambda}^{e\,tr}_{A\,n+1} := \left(J^{e\,tr}_{n+1}\right)^{-1/3} \lambda^{e\,tr}_{A\,n+1} .$$

2. *Trial state:*

2.1. Compute the trial principal effective Kirchhoff stresses (e.g. Hencky's law), decomposed in their deviatoric component $\beta^{tr}_{A\,n+1}$ and volumetric component $\bar{\tau}^{tr}_{n+1}$

$$\beta^{tr}_{A\,n+1} = 2\mu_{sk}\log\bar{\lambda}^{e\,tr}_{A\,n+1} \quad (A = 1,3) \quad \text{and} \quad \bar{\tau}^{'\,tr}_{n+1} = \kappa_{sk}\log J^{e\,tr}_{n+1} .$$

The plastic flow is fixed, i.e., $\alpha^{tr}_{n+1} = \alpha_{n+1}$ and $M^{p\,tr}_{n+1} = M^p_n$.

2.2. Compute the trial yield condition

$$\Phi^{tr}_{n+1} = \frac{1}{\sqrt{2}}\Bigg(\underbrace{\sqrt{\sum_{A=1}^{3}\left(\beta^{tr}_{A\,n+1}\right)^2}}_{\|\operatorname{dev}\boldsymbol{\tau}^{'\,tr}_{n+1}\|} + g(\bar{\tau}^{'\,tr}_{n+1})\Bigg) - [\tau_{yo} - q(\alpha_n)]$$

where $q(\alpha_n)$ corresponds to the hardening/softening law.

3. *Check consistency of the trial step:*

```
IF  (Φ^tr_{n+1} ≤ 0) THEN
    ELASTIC STEP: Update internal variables and stresses  (·)_{n+1} = (·)^tr_n
    GOTO 5
ELSE
    PLASTIC STEP
ENDIF
```

BOX I.1b. (cont.) Return mapping algorithm for the generalized Drucker-Prager poro-plastic model summarized in Box 3.1.

4. *Plastic step:*

4.1. Solve for the consistency parameter $\Delta\gamma$ and the effective volumetric stress $\bar{\tau}'_{n+1}$

$$\left.\begin{aligned} r_{\Phi_{n+1}} &:= \frac{1}{\sqrt{2}}\Big(\| \operatorname{dev} \boldsymbol{\tau}'^{\,tr}_{n+1}\| + g(\bar{\tau}'_{n+1})\Big) - [\tau_{yo} - q(\alpha_{n+1})] - 2\mu_{sk}\Delta\gamma = 0 \\ r_{\bar{\tau}'_{n+1}} &:= \bar{\tau}'_{n+1} - \bar{\tau}'^{\,tr}_{n+1} + \frac{\Delta\gamma}{\sqrt{2}}\,\kappa_{sk}\,g'(\bar{\tau}'_{n+1}) = 0 \end{aligned}\right\}$$

where $\alpha_{n+1} = \alpha^{tr}_n + \Delta\gamma$. This system of equations is solved using Newton's scheme

$$\left.\begin{aligned} &\Delta\gamma^{(k+1)} = \Delta\gamma^{(k)} + \delta\,(\Delta\gamma)^{(k+1}\ , \qquad \bar{\tau}'^{\,(k+1)}_{n+1} = \bar{\tau}'^{\,(k)}_{n+1} + \delta(\bar{\tau}'_{n+1})^{(k+1)}\ , \\ &\delta\,(\Delta\gamma)^{(k+1)} = \left[r^{(k)}_{\Phi_{n+1}} - \frac{g'^{(k)}}{\sqrt{2}\,\Theta^{(k)}_{n+1}}\,r^{(k)}_{\bar{\tau}'_{n+1}}\right] \Bigg/ \left[2\mu_{sk} + H^{(k)} + \frac{\kappa_{sk}\left(g'^{(k)}\right)^2}{2\,\Theta^{(k)}_{n+1}}\right] \\ &\delta(\bar{\tau}'_{n+1})^{(k+1)} = -\frac{1}{\Theta^{(k)}_{n+1}}\left[r^{(k)}_{\bar{\tau}'_{n+1}} + \frac{\kappa_{sk}g'^{(k)}}{\sqrt{2}}\delta(\Delta\gamma)^{(k+1)}\right]\ , \end{aligned}\right\}$$

where $\Theta^{(k)}_{n+1} := 1 + \Delta\gamma^{(k)}\ \kappa_{sk}g''^{(k)}/\sqrt{2}$, and $H^{(k)} = -\frac{dq}{d\alpha}\Big|_{\alpha^{(k)}_{n+1}}$ with $\alpha^{(k)}_{n+1} = \alpha^{tr}_{n+1} + \Delta\gamma^{(k)}$, for each iteration $k = 0, 1, 2, \ldots$ $(\Delta\gamma^{(0)} = 0)$.

4.2 Update the internal variables and compute the effective stresses:

$$\beta_{A\,n+1} = \beta^{tr}_{A\,n+1}\left[1 - \frac{\sqrt{2}\,\Delta\gamma\,\mu_{sk}}{\| \operatorname{dev}\boldsymbol{\tau}^{tr}_{n+1}\|}\right]\ , \quad \bar{\lambda}^{e}_{A\,n+1} = \bar{\lambda}^{e\,tr}_{A\,n+1}\exp\left[\frac{\beta_{A\,n+1}}{2\mu_{sk}}\right] \quad (A = 1, 3)\ ,$$

$$J^{e}_{n+1} = J^{e\,tr}_{n+1}\exp\left[-\frac{\Delta\gamma}{\sqrt{2}}\,g'(\bar{\tau}'_{n+1})\right]\ , \quad \alpha_{n+1} = \alpha^{tr}_{n+1} + \Delta\gamma \quad \text{and}$$

$$M^{p}_{n+1} = M^{p\,tr}_{n+1} + b\,\rho_{w_o}\log\left(\frac{J_{n+1}J^{e}_{n}}{J^{e}_{n+1}\,J_n}\right)\ .$$

Compute $\lambda^{e}_{A\,n+1} = (J^{e}_{A\,n+1})^{(1/3)}\bar{\lambda}^{e}_{A\,n+1}$, $\boldsymbol{b}^{e}_{n+1} = \sum_{A=1}^{3}\lambda^{e}_{A\,n+1}\boldsymbol{n}^{tr}_{A\,n+1}\otimes\boldsymbol{n}^{tr}_{A\,n+1}$, and

$$\boldsymbol{\tau}'_{n+1} = \sum_{A=1}^{3}\beta_{A\,n+1}\boldsymbol{n}^{tr}_{A\,n+1}\otimes\boldsymbol{n}^{tr}_{A\,n+1} + \bar{\tau}'_{n+1}\,\mathbf{1}\ .$$

5. *Compute the total stresses with updated pore pressure:*

$$\boldsymbol{\tau} = \boldsymbol{\tau}' - b\,\rho_{w_o}\ (\mu_w(\tilde{p}) - \mu_{w_o})\ \mathbf{1}\ ,$$

where $\tilde{p} = p_{n+1}$ for the monolithic scheme, $\tilde{p} = p_n$ for the drained split, and for the undrained split $\tilde{p}$ is obtained by solving locally at each Gauss point equation (I.7) using Newton's method.

BOX I.2. Consistent tangent for the return mapping algorithm summarized in Box I.1.

Exact consistent algorithmic tangent:

$$\boxed{\mathbf{c}_{n+1} = \sum_{A=1}^{3}\sum_{B=1}^{3} a^{ep}_{AB\,n+1}\boldsymbol{m}^{tr\,(A,A)}_{n+1} \otimes \boldsymbol{m}^{tr\,(B,B)}_{n+1} + \boldsymbol{g}^{tr}_{n+1}\ ,}$$

where $$\boldsymbol{m}^{tr\,(A,B)}_{n+1} := \tfrac{1}{2}\left[\boldsymbol{n}^{tr\,(A)}_{n+1} \otimes \boldsymbol{n}^{tr\,(B)}_{n+1} + \boldsymbol{n}^{tr\,(B)}_{n+1} \otimes \boldsymbol{n}^{tr\,(A)}_{n+1}\right]\ .$$

The moduli $\boldsymbol{g}^{tr}_{n+1}$ are independent of the plasticity model and are given by

$$\boxed{\begin{aligned}\boldsymbol{g}^{tr}_{n+1} = &\sum_{A=1}^{3}(-2\tau_{A\,n+1})\ \tfrac{1}{2}\left[\boldsymbol{m}^{tr\,(A,A)}_{n+1} \otimes \boldsymbol{m}^{tr\,(A,A)}_{n+1} + \boldsymbol{m}^{tr\,(A,A)}_{n+1} \otimes \boldsymbol{m}^{tr\,(A,A)}_{n+1}\right]\\ &+ \sum_{\substack{A,B=1\\ A\neq B}}^{3} \frac{\tau^{tr}_{A\,n+1}\ \left(\lambda^{e\,tr}_{B\,n+1}\right)^2 - \tau^{tr}_{B\,n+1}\ \left(\lambda^{e\,tr}_{A\,n+1}\right)^2}{\left(\lambda^{e\,tr}_{A\,n+1}\right)^2 - \left(\lambda^{e\,tr}_{B\,n+1}\right)^2}\ \boldsymbol{m}^{tr\,(A,B)}_{n+1} \otimes \boldsymbol{m}^{tr\,(B,A)}_{n+1}\end{aligned}}$$

where $\tau_{A\,n+1} = \beta_{A\,n+1} + \bar{\tau}'_{n+1} - b\ \rho_{w_o}\ (\mu_w(\tilde{p}) - \mu_{w_o})$. The elastoplastic contributions are given by

i. *Elastic step:*

$$\boxed{\boldsymbol{a}^{ep}_{n+1} = [\kappa_{sk} + \pi]\ \widehat{\boldsymbol{e}} \otimes \widehat{\boldsymbol{e}} + 2\mu_{sk}\ [\mathbf{1} - \frac{1}{3}\widehat{\boldsymbol{e}} \otimes \widehat{\boldsymbol{e}}]}$$

where $\widehat{\boldsymbol{e}} = [1\ 1\ 1]^T$, $\mathbf{1}$ = identity 3×3 matrix, and π is defined below.

ii. *Plastic step:*

$$\boxed{\begin{aligned}\boldsymbol{a}^{ep}_{n+1} = &\left[\kappa_{sk}\left(1 - \frac{(g')^2\kappa_{sk}}{2\,\Theta_{n+1}\,\Xi_{n+1}}\right) + \pi\right]\ \widehat{\boldsymbol{e}} \otimes \widehat{\boldsymbol{e}} - \frac{\sqrt{2}\mu_{sk}\kappa_{sk}g'}{\Theta_{n+1}\,\Xi_{n+1}}\ \widehat{\boldsymbol{s}}_{n+1}\\ &+ 2\mu_{sk}\ \left(1 - \frac{\sqrt{2}\ \Delta\gamma\ \mu_{sk}}{\|\operatorname{dev}\boldsymbol{\tau}^{tr}_{n+1}\|}\right)\ \left[\mathbf{1} - \frac{1}{3}\widehat{\boldsymbol{e}} \otimes \widehat{\boldsymbol{e}}\right]\\ &- 2\mu_{sk}\ \left(\frac{2\mu_{sk}}{\Xi_{n+1}} - \frac{\sqrt{2}\ \Delta\gamma\ \mu_{sk}}{\|\operatorname{dev}\boldsymbol{\tau}^{tr}_{n+1}\|}\right)\ \widehat{\boldsymbol{m}}_{n+1} \otimes \widehat{\boldsymbol{m}}_{n+1}\end{aligned}}$$

$$(\widehat{\boldsymbol{m}}_{n+1})_A = \frac{1}{\|\operatorname{dev}\boldsymbol{\tau}_{n+1}\|}\ \beta_{A\,n+1}\ , \qquad (\widehat{\boldsymbol{s}}_{n+1})_{AB} = \frac{1}{\|\operatorname{dev}\boldsymbol{\tau}_{n+1}\|}\ [\beta_{A\,n+1} + \beta_{B\,n+1}]\ ,$$

$$\Theta_{n+1} = 1 + \frac{\Delta\gamma}{\sqrt{2}}\ \kappa_{sk}g''\ , \qquad \Xi_{n+1} = 2\mu_{sk} + H_{n+1} + \frac{\kappa_{sk}\ (g')^2}{2\,\Theta_{n+1}}$$

In the above expressions $\pi = 0$ for the monolithic scheme and drained split, whereas for the undrained split $\pi = b^2\ Q$, leading to the undrained elasticities.